

**2015 年度**

**大阪産業大学大学院 工学研究科**

**博士前期課程 情報システム工学専攻**

**修士論文**

---

**題名 Tomographic PIV analysis on the behavior of  
water-tornado flow rise in Powered water Circulatory System**

---

**主査 近江 和生 教授**

**副査 後藤 彰彦 教授**

**副査 宇佐美 清章 教授**

**副査**

**著者氏名（学籍番号） TULADHAR SUDAT**

**(14MH03)**

---

**提出日 2016 年 1 月 19 日**

# **Tomographic PIV analysis on the behavior of water-tornado flow rise in Powered water Circulatory System**



**TULADHAR SUDAT**

**(14MH03)**

Graduate School of Engineering

Osaka Sangyo University

Osaka, Japan

A thesis submitted for the degree of

*Master of Engineering*

March 2016

## **Acknowledgements**

I would like to express my sincere and deepest gratitude to Prof. Kazuo Ohmi and Prof. Akira Hiratsuka for their valuable guidance throughout the study period.

I am deeply grateful to Prof. Akihiko Goto and Prof. Kiyoaki Usami who have given their valuable time and effort to read through the thesis and for their constructive inputs.

I am very much thankful to the Ministry of Education, Culture, Sports, Science and Technology of Japanese Government for the financial support during the study period.

Lastly, I would like to thank Mr. Yoichi Kamitani and Mr. Naoki Lee for their support in the experiments. Also thanks to all other friends, colleagues and classmates whose sincere efforts have inspired me to pursue my academic goals.

# **Abstract**

Flow visualization technique using Particle Image Velocimetry (PIV) is a widely accepted field measuring technique to study the characteristics of fluid flow in hydrodynamic research, modern aerodynamics and industrial applications. Among various PIV techniques (stereoscopic PIV, Dual plane stereoscopic PIV, Micro-PIV, Holographic) for fluid flow measurement, Tomographic-PIV is a digital 3D measurement system that combines the simple optical arrangement of the photogrammetric approach with a robust particle volume reconstruction procedure. It uses the principle of Multiplicative and Additive Reconstruction Technique (MART) to reconstruct the 3D position of the particles in the flow and then cross-correlation templating matching techniques to estimate the displacement and thus velocity and vorticity of fluid flow.

From the viewpoint of global environmental protection, the promotion of circulation of deoxygenated bottom layer water in closed water areas (lakes, ponds and reservoirs) is an important issue to be considered. Many conventional solutions use gigantic physical or chemical techniques of water. One of the recent techniques is Powered water Circulatory System (PCS). It is a simple and energy efficient solution that uses an artificial tornado flow generated by a rotating subsurface impeller. Some previous works provide the two dimension-three component (2D-3C) analysis of tornado flow in such systems but to understand the full dynamics a complete three dimension-three component (3D-3C) analysis is further required. Also the optimum value of system design parameters (motor speed and immersed value) is still unknown for maximizing the tornado flow-rise and minimizing surrounding spread or mix.

In the present study, the flow pattern of the artificial water tornado in a PCS is investigated by 3D tomographic PIV experiments and flow visualization technique to understand the vortex flow development in a tornado for efficient pump-up circulation under various design parameters of the system. A complete 3D-3C analysis of the flow structures of tornado flow around the tornado boundary and in the surrounding is presented. Cross-sectional analysis of the tornado rise at various experimental conditions is analyzed to obtain optimum design parameters (motor speed and immersed impeller depth) for the most efficient conditions for efficient pump-up (extraction) and minimum spread (mix).

# Table of Contents

Acknowledgements

Abstract

List of Figures

List of Abbreviations

<b>1. Introduction .....</b>	<b>1</b>
1.1. PIV basics.....	1
1.2. PIV techniques .....	2
1.3. Three dimension (3D) and Three component (3C) .....	3
1.4. Power Circulatory System (PCS).....	4
1.5. Problem statement .....	5
1.6. Objectives of the research .....	6
1.7. Brief overview of the thesis .....	6
<b>2. Theory and Algorithms .....</b>	<b>7</b>
2.1. Calibration.....	7
2.1.1. Pinhole Camera Model.....	7
2.1.2. Direct Linear Transformation (DLT) .....	8
2.2. Principles of Tomographic-PIV .....	11
2.3. Tomographic reconstruction algorithm .....	12
2.3.1. MART.....	14
2.3.2. Weight Estimation.....	14
2.4. Displacement vector .....	16
2.5. Flow velocity and vorticity .....	18
2.6. Gaussian mask cross correlation (GMCC) .....	19
2.7. Sub-Pixel Estimation .....	20
<b>3. Research Methodology.....</b>	<b>22</b>
3.1. Experimental setup .....	22
3.2. Calibration Procedure .....	23
3.3. Experiment parameters .....	25

<b>4. Results and Discussions .....</b>	<b>27</b>
4.1. Calibration Accuracy .....	27
4.2. Raw Images .....	27
4.3. Voxel (Positional) reconstructions .....	28
4.4. Velocity reconstructions .....	30
4.4.1. 3D-3C Reconstruction .....	30
4.4.2. Tornado flow temporal characteristics at a fixed height.....	31
4.4.3. Tornado flow characteristics at various heights .....	33
4.5. Effects of motor speed.....	36
4.6. Effects of immersed impeller depth .....	40
<b>5. Conclusions.....</b>	<b>43</b>

## **References**

# List of Figures

1.1	Overview of a PIV system	2
1.2	Three dimensions (3D) and three components (3C)	3
1.3	Various flow profiles	4
1.4	Powered water circulatory system (PCS)	5
1.5	Time evolution of water tornado flow	6
2.1	Pinhole Camera Model	7
2.2	Camera parameters relation	8
2.3	Object space and image plane reference frames and associated coordinate system	9
2.4	Projection of object space onto image plane	10
2.5	Tomographic-PIV principle	11
2.6	Imaging model used for tomographic reconstruction	13
2.7	Formation of ghost particles in a 2 camera setup	13
2.8	MART reconstruction	14
2.9	Weight coefficient estimation	15
2.10	Cross correlation analysis using template matching method	16
2.11	Parallel projection correlation	17
2.12	Examples of some zero and non-zero vorticity	18
2.13	2D gaussian distribution	19
2.14	Gaussian distribution (point spread function and kernel)	20
2.15	Three-point Gaussian fit for sub-pixel estimation	21
3.1	Schematics of experimental setup	23
3.2	Calibration plate	24
3.3	Raw Images of calibration plate taken from three viewing cameras	24
3.4	Excel verification of detection of dot-order for one of the calibration image	25
4.1	Calibration Error for 3D reconstruction	27
4.2	Raw images of tornado flow taken from three different viewing cameras	28
4.3	Voxel (3D positional) reconstruction	29
4.4	Tomographic reconstructions at different stages	29
4.5	3D 3C displacement reconstruction	31
4.6	Time evolution of tornado flow-rise of the reconstructed displacement vectors	33
4.7	Tornado flow-rise at different height sections for a water-tornado at a single time instant	35
4.8	Tornado flow-rise at different motor speed	39
4.9	Tornado flow-rise at different immersed impeller depth	41

# List of Abbreviations

2D/3D	Two-Dimension/Three-Dimension
2C/3C	Two-Component/Three-Component
ART	Algebraic Reconstruction Technique
CCD	Charged Couple Devices
DLT	Direct linear Transformation
GMCC	Gaussian Mask Cross Correlation
LOS	Line of Sight
MART	Multiplicative Algebraic Reconstruction Technique
PCS	Powered water Circulatory System
PIV	Particle Image Velocimetry
PPC	Parallel Projection Correlation
PTV	Particle Tracking Velocimetry
RPM	Revolution per Minute

# 1. Introduction

Flow visualization of the fluid dynamics is very important to study hydrodynamic research (weather and climate patterns), modern aerodynamics (airplanes, ships and land vehicles) and optimum industrial machinery that generate fluid flows. A hot-wire anemometry is one of the most traditional intrusive technique to measure the quantitative information of the flow field. But due to advancement of digital image processing techniques together with electronic and optical hardware, a non-intrusive optical technique called laser Doppler anemometer is more efficient. Because both of these techniques only provide the flow information at a point, an image-based flow field technique called Particle Image Velocimetry (PIV) is much popular. This technique provides two or three-dimensional velocity maps for flows based on the images captured by different viewing cameras, of the light scattered by small particles in the flow, illuminated by a laser light sheet.

## 1.1. PIV basics

A typical PIV system consists of two parts: (a) image capture system for capturing the images of the tracer particles in a fluid flow and (b) post processing PIV analysis to obtain the information such as velocity and vorticities at different regions in the fluid flow.

In the image capture system, tracer particles within the test volume are illuminated by a laser light sheet of certain thickness produced by a high energy pulsed laser as shown in Fig 1.1. The two-dimensional (2D) images of the projections of the illuminated three-dimensional (3D) scene are captured by two or more cameras viewing from different directions. The cameras take the pictures of the double-exposed individual particles. The images are captured on a Charged Couple Device (CCD) of a camera which is subsequently transferred to a storing Personal Computer (PC) for further analysis.

In the post processing PIV analysis, double-exposed individual particles which are assumed to faithfully follow the flow movement, are compared with each other to find relative movement of the fluid flow at every location of the scene. At first, the position of particles in the first and second time steps  $t$  and  $t+\Delta t$  is determined using various reconstruction techniques such as algebraic reconstruction. Then the best match between sections of the first and second scene is determined using various matching algorithms such as cross-correlation. This gives the displacement of particles at various sections of the flow. With known pulse separation and a measured particle displacement, velocity and thus vorticity values are determined.

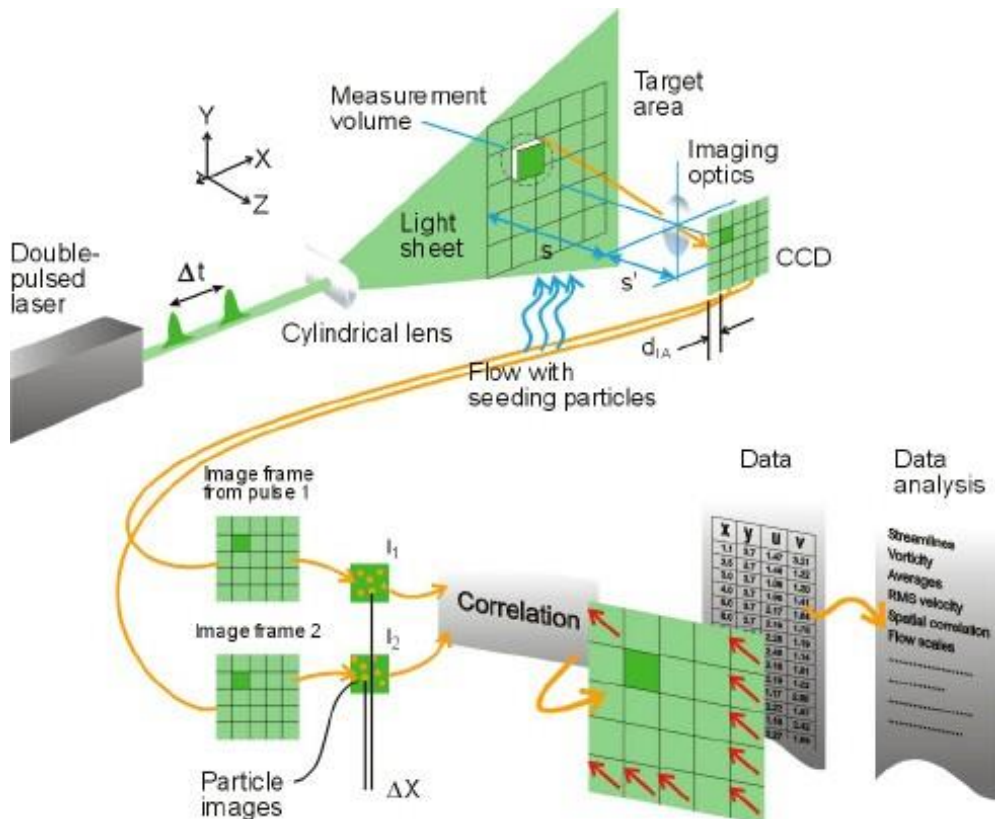


**Fig 1.1** Overview of a PIV system (Courtesy: Dantec Dynamics)

## 1.2. PIV techniques

Various PIV techniques have been developed to study the 2D and 3D flow fields. Some of the techniques are:

### Stereoscopic PIV

Stereoscopic PIV uses two cameras with separate viewing angles to extract the z-axis displacement. Both cameras must be focused on the same spot in the flow and must be properly calibrated to have the same point in focus.

### Dual plane stereoscopic PIV

Dual plane stereoscopic PIV is an expansion of stereoscopic PIV by adding a second plane of investigation directly offset from the first one. Four cameras are required for this analysis. The two planes of laser light are created by splitting the laser emission with a beam splitter into two beams. Each beam is then polarized orthogonally with respect to one another. Next, they are transmitted through a set of optics and used to illuminate one of the two planes simultaneously.

### Micro-PIV

Micro-PIV uses fluorescing particles excited at a specific wavelength and emitted at another wavelength. While PIV draws its 2-dimensional analysis properties from the planar nature of the laser sheet, micro-PIV utilizes the ability of the objective lens to focus on only one plane at a time, thus creating a 2-dimensional plane of viewable particles.

# Holographic PIV

Holographic PIV uses the interference of coherent light scattered by a particle and a reference beam to encode information of the amplitude and phase of the scattered light incident on a sensor plane. This encoded information, known as a hologram, can then be used to reconstruct the original intensity field by illuminating the hologram with the original reference beam via optical methods or digital approximations.

# Tomographic PIV

The Tomographic-PIV technique (Elsinga et. al. [1]) is a digital 3D measurement system that combines the simple optical arrangement of the photogrammetric approach with a robust particle volume reconstruction procedure, which does not rely on particle identification. As a consequence the seeding density can be increased, with respect to Particle Tracking Velocimetry (PTV), to around 0.05 particles per pixel. The robustness of the velocimetry technique is further increased by applying particle pattern cross-correlation instead of individual particle tracking. Tomography itself has been used for various other applications like medical (Magnetic resonance imaging, MRI and study of vortex formation in prosthetic heart valves), industrial manufacturing (accurate positioning of robots), aerodynamics (study of flow over an aircraft wing in a wind tunnel), atmospheric science (weather) etc.

### 1.3. Three dimension (3D) and Three component (3C)

Three dimensions (3D) generally describe a volume that provides the perception of depth. For a fluid flow profile to be available in 3D, it must have its velocity values at certain interval in all length, breadth and height directions as shown in Fig 1.2(a). Three components (3C) generally describe three vector dimensions at each position of a 3D space as shown in Fig 1.2(b). Flow profiles can be 2D-2C, 2D-3C, 3D-2C or 3D-3C as shown in Fig 1.3.

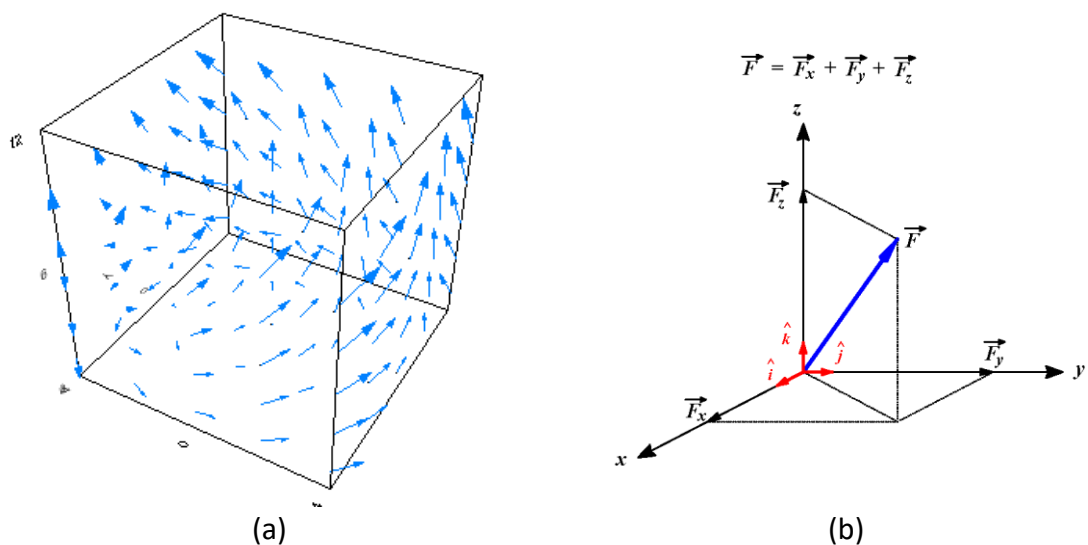


**Fig 1.2** Three dimensions (3D) and three components (3C)

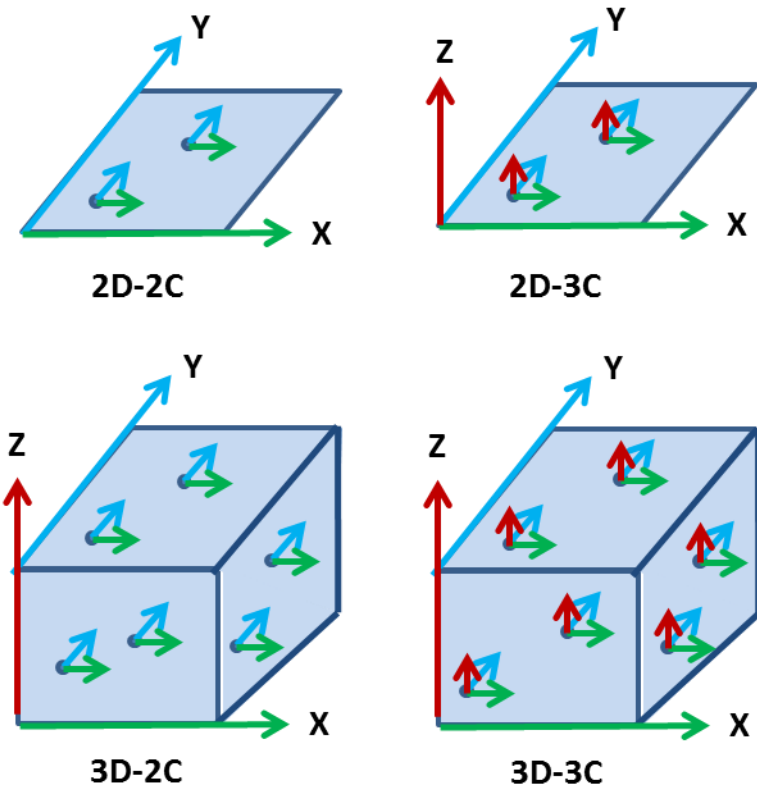


**Fig 1.3** Various flow profiles

#### 1.4. Power Circulatory System (PCS)

In closed water areas, because of the inflow of sand, mud, chlorides of nitrogen and phosphorous, the water density is stratified in depth direction and the bottom water is highly stagnant and deoxygenated. And in such environment the generation of microcysts and other types of contaminants due to the stagnancy and eutrophication of the bottom layer water becomes a serious problem (Hiratsuka and Ishikawa [2]) causing poor oxygenation of low rise water and deterioration of water environment. So the circulation of this deoxygenated bottom water and removal of bottom sediments is an important issue for global environment protection and purification. In order to address this problem, a couple of physicochemical techniques have been introduced so far to improve and purify the water quality. These techniques include (a) bottom layer aeration and water circulation, (b) oxidization of bottom sediments by using air pumps, and (c) bottom sediments removal (dredge). There is however concern that such techniques, especially the last measure, may cause another type of water contamination due to the stir up of bottom sediments or even the increase of mélange of bottom sediment due to the biodegradation in water. Furthermore, from the viewpoint of landscape preservation as well, reasonable and efficient removal of bottom sediments in closed water areas must be another important issue.

One of the new measures for this environmental problem used practically in these days is the Powered water Circulator System (PCS) (Hanari and Sakakibara [3]; Ohmi et al. [4]) that is installed above the water surface. In the real scenario, the system repeatedly operates on different cross-section of a water source (river, pond, lake etc.) extracting the sediments

every section. The system can pump up the bottom water by generating an artificial tornado-like rising current through a submerged impeller. The lower part of this impeller, composed of normal inclined vanes for axial flow, pumps up the water from below, while the upper part of the impeller, composed of vertical vanes for radial flow, ejects the pumped water in the radial direction (EcoFlow Document [5]). However, since this method also agitates the bottom layer water towards the upper surface and radiates it in all directions, it may cause a new pollution problem. Therefore, in order to prevent such water pollution, some energy efficient recovery technique is necessary for efficient collection of bottom sediments and contaminants diffused by this water circulator system.

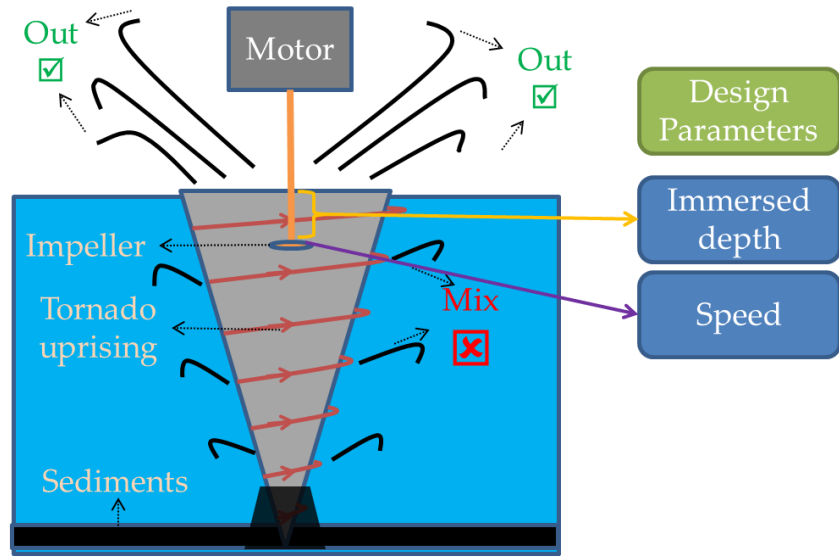


**Fig 1.4** Powered water circulatory system (PCS)

The physical design parameters of the system namely (a) immersed depth to water tank height ratio,  $d/H$  and (b) the rotation speed (rpm) of the impeller motor as shown in Fig 1.4 play a vital role in the creation, sustainability and efficient pump-up of the water.

## 1.5. Problem statement

Stereoscopic 2D-3C PIV study of tornado flow (Sakakibara [3]) provides some information on axial velocity fluctuation but more detailed 3D-3C analysis is required to determine full tornado rise flow behavior. It is found from flow visualization experiment on water tornado (Fig 1.5) that the water tornado after generation evolves with a highly characteristic vortex flow so that further 3D-3C flow analysis of such a flow is necessary to know physical mechanism of vortex development and decay in the tornado and to improve the efficiency of pump-up circulation. Also the optimized value for the system design parameters (motor speed and immersed impeller depth) for efficient tornado-rise and minimum spread (mix) needs to be investigated by flow visualization technique.



**Fig 1.5 Time evolution of water tornado flow**

## 1.6. Objectives of the research

The research aims to perform 3D-3C analysis on the behavior of water tornado flow rise in Powered water Circulatory System using Tomographic PIV and use the visualization technique to understand vortex flow development in a tornado for efficient pump-up circulation under various design parameters of the system.

## 1.7. Brief overview of the thesis

In the present study, the author is involved mainly in the flow mechanism analysis of the tornado-like rising current, while referring to the earlier works of Hanari and Sakakibara [3]. The experimental approach of the present study is flow visualization by 3D tomographic Particle Image Velocimetry (PIV). The flow analysis in the present study will be carried out with the aim of optimized pump-up of bottom water for efficient collection of bottom sediments and contaminants.

Chapter 2 describes the background theory and the mathematical formulation of the algorithms used in tomographic PIV. Camera calibration model, Direct Linear Transformation (DLT) with Multiplicative Algebraic Reconstruction Technique (MART) for tomographic reconstruction and 3D cross correlation analysis for displacement and velocity measurements are explained. The Gaussian Mask Cross Correlation (GMCC) for particle detection and three-point gaussian fitting for sub-pixel accuracy are also described in this chapter.

Chapter 3 presents the results of the thesis. A detail analysis of the tornado-rise fluid flow in a Powered water Circulatory System is described along with some tornado features such as vortex characteristics, rise and spreading. This chapter also presents results on the effect of physical experiment parameters (motor speed and immersed impeller depth) and discusses the optimum conditions for efficient extraction of bottom sediments.

Finally Chapter 4 concludes the research work and presents conclusion of the thesis.

## 2. Theory and Algorithms

### 2.1. Calibration

Camera calibration is a process of estimating the parameters of a lens and image sensor of a camera. These parameters are used to correct for lens distortion, measure the size of an object in world units or determine the location of the camera in a scene. It is used in applications such as machine vision to detect or measure objects and in robots for navigation. This is a very important process for finding the parameters of the camera and the 3D scenario for later PIV analysis.

The camera calibration techniques (Zhang [6]) involve estimating camera parameters using a 3D world points and their corresponding 2D image points. These correspondences are obtained using images of a calibration pattern (checkboard or a dot pattern) from all the viewing cameras. The camera parameters solved using these correspondences can be used to evaluate the accuracy of calibration as

- Verifying the location of camera and the calibration pattern
- Calculating the re-projection errors

Camera parameters include intrinsic, extrinsic and distortion coefficients. To determine the camera parameters, a camera model is required that includes pinhole camera model (Computer Vision Courses [7]) and lens distortion. Radial and tangential lens distortion is to be taken into account for more accurate representation of a real camera.

#### 2.1.1. Pinhole Camera Model

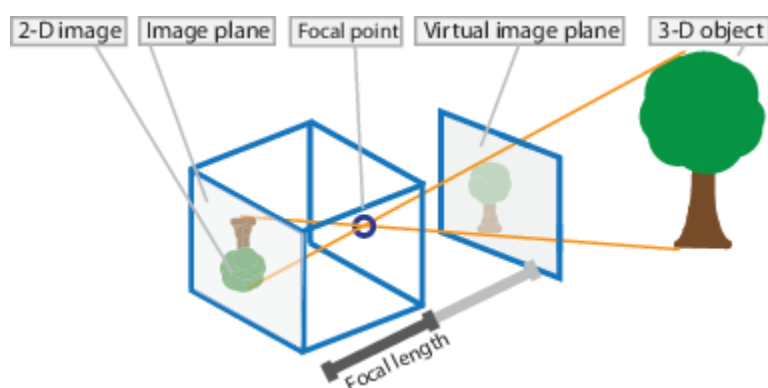


**Fig 2.1** Pinhole Camera Model

A pinhole camera is a simple camera without a lens and with a single small aperture. Light rays pass through the aperture and project an inverted image on the opposite side of the camera as shown in Fig. 2.1.

The pinhole camera parameters are represented by a  $4 \times 3$  matrix called a camera matrix. This matrix maps the 3D world scene into the image plane. The calibration algorithm calculates the camera matrix using the extrinsic and intrinsic parameters. The extrinsic parameters represent the location of the camera in the 3D scene. The intrinsic parameters represent the optical center and focal length of the camera. The model can be described as

$$w [x \ y \ 1] = [X \ Y \ Z \ 1] \ P$$

Scale factor      Image points      World points  
 $P = [R \ t] K$   
 Camera matrix      Extrinsic      Intrinsic matrix  
 Rotation and translation

In the model, camera matrix  $P$  consisting of extrinsic parameters (rotation and translation) and intrinsic parameters (focus and distortion) is used to transform world points to camera coordinates and then map into the image plane as shown in Fig 2.2. The extrinsic parameters represent a rigid transformation from 3D world coordinate system to the 2D camera coordinate system. The intrinsic parameters represent a projective transformation from the 3-D camera's coordinates into the 2-D image coordinates.

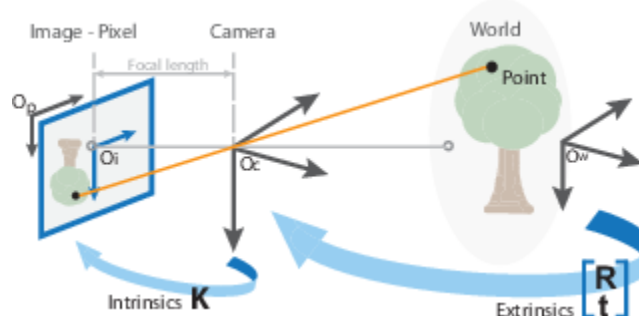


**Fig 2.2** Camera parameters relation

### 2.1.2. Direct Linear Transformation (DLT)

Direct linear transformation (DLT) (kwon3d courses [\[8\]](#)) is a method of determining the 3-D location of an object (or points on an object) in space using two or more views of the object. DLT method uses a set of control points whose object space/plane coordinates are already known. The control points are normally fixed to a rigid frame called calibration plate. The flexibility of the DLT calibration is its ease at handling the calibration plate.

In the DLT calibration model, the image coordinate  $(u, v)$  is modelled as a function of world point  $(x, y, z)$  as

$$u = \frac{L_1x + L_2y + L_3z + L_4}{L_9x + L_{10}y + L_{11}z + 1} \quad (2.1)$$

$$v = \frac{L_5x + L_6y + L_7z + L_8}{L_9x + L_{10}y + L_{11}z + 1} \quad (2.2)$$

, where  $L_n = [L_1 \sim L_{11}]$  is standard DLT calibration parameters of a single camera that maps the 3D world points to 3D camera homogeneous coordinate system. Based on the projection of known point on an object in 3D space onto three camera image planes as shown in Fig 2.3, DLT calibration parameters  $L_n$  for each of three camera is obtained namely  $L_n^{[1]}$ ,  $L_n^{[2]}$  and  $L_n^{[3]}$ . Equation (2.1) and (2.2) is used to transform 3D world point to 2D image co-ordinates of corresponding cameras.

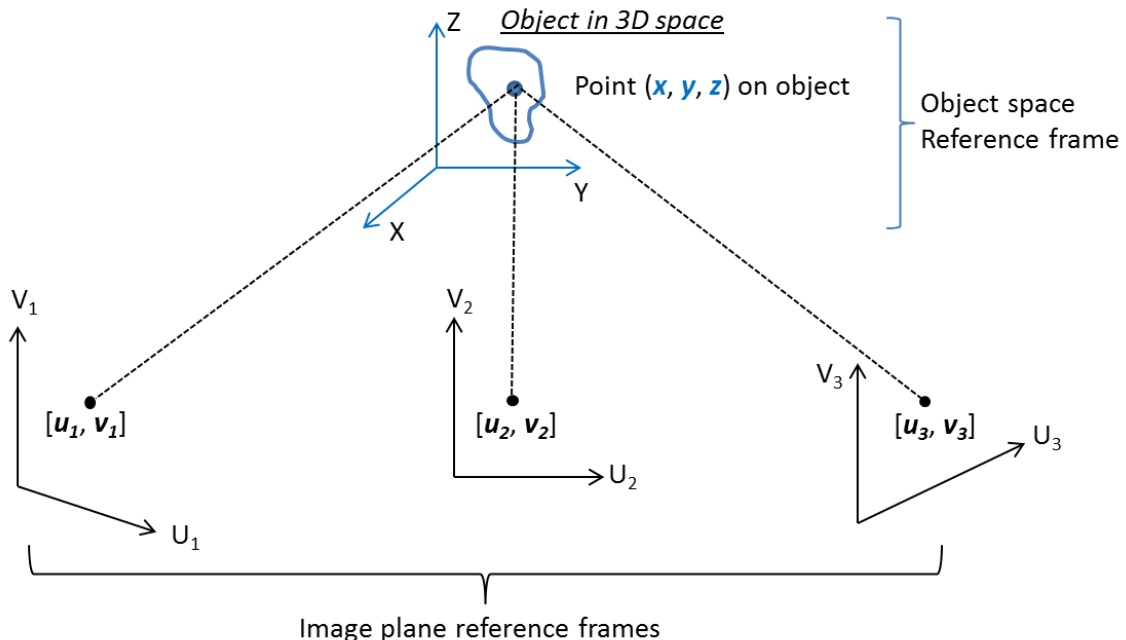


**Fig 2.3** Object space and image plane reference frames and associated coordinate system

The camera parameter  $L_n$  in DLT is calculated using the  $n$  known control points as

$$\begin{bmatrix} \frac{x_1}{R_1} & \frac{y_1}{R_1} & \frac{z_1}{R_1} & \frac{1}{R_1} & 0 & 0 & 0 & 0 & \frac{-u_1x_1}{R_1} & \frac{-u_1y_1}{R_1} & \frac{-u_1z_1}{R_1} \\ 0 & 0 & 0 & 0 & \frac{x_1}{R_1} & \frac{y_1}{R_1} & \frac{z_1}{R_1} & \frac{1}{R_1} & \frac{-v_1x_1}{R_1} & \frac{-v_1y_1}{R_1} & \frac{-v_1z_1}{R_1} \\ \vdots & \vdots \\ \frac{x_n}{R_n} & \frac{y_n}{R_n} & \frac{z_n}{R_n} & \frac{1}{R_n} & 0 & 0 & 0 & 0 & \frac{-u_nx_n}{R_n} & \frac{-u_ny_n}{R_n} & \frac{-u_nz_n}{R_n} \\ 0 & 0 & 0 & 0 & \frac{x_n}{R_n} & \frac{y_n}{R_n} & \frac{z_n}{R_n} & \frac{1}{R_n} & \frac{-v_nx_n}{R_n} & \frac{-v_ny_n}{R_n} & \frac{-v_nz_n}{R_n} \end{bmatrix} \begin{bmatrix} L_1 \\ L_2 \\ \vdots \\ L_{10} \\ L_{11} \end{bmatrix} = \begin{bmatrix} \frac{u_1}{R_1} \\ \frac{v_1}{R_1} \\ \vdots \\ \frac{u_n}{R_n} \\ \frac{v_n}{R_n} \end{bmatrix} \quad (2.3)$$

, where

$$R_n = L_9 x_n + L_{10} y_n + L_{11} z_n + 1 \quad (2.4)$$

The equation is solved using least square method for overdetermined system since we have  $2n = 2 \times 120 = 240$  equations with  $3 \times 11 = 33$  unknowns. After determining the DLT parameters  $L_n^{(m)}$  for all  $m$  cameras, 3D world point  $[x, y, z]$  correspondence for image coordinate location of the same 3-D world point  $[(u^{(1)}, v^{(1)}), (u^{(2)}, v^{(2)}) \dots (u^{(m)}, v^{(m)})]$  is determined as

$$\begin{bmatrix} \frac{u^{(1)}L_9^{(1)} - L_1^{(1)}}{R^{(1)}} & \frac{u^{(1)}L_{10}^{(1)} - L_2^{(1)}}{R^{(1)}} & \frac{u^{(1)}L_{11}^{(1)} - L_3^{(1)}}{R^{(1)}} \\ \frac{v^{(1)}L_9^{(1)} - L_5^{(1)}}{R^{(1)}} & \frac{v^{(1)}L_{10}^{(1)} - L_6^{(1)}}{R^{(1)}} & \frac{v^{(1)}L_{11}^{(1)} - L_7^{(1)}}{R^{(1)}} \\ \vdots & \vdots & \vdots \\ \frac{u^{(m)}L_9^{(m)} - L_1^{(m)}}{R^{(m)}} & \frac{u^{(m)}L_{10}^{(m)} - L_2^{(m)}}{R^{(m)}} & \frac{u^{(m)}L_{11}^{(m)} - L_3^{(m)}}{R^{(m)}} \\ \frac{v^{(m)}L_9^{(m)} - L_5^{(m)}}{R^{(m)}} & \frac{v^{(m)}L_{10}^{(m)} - L_6^{(m)}}{R^{(m)}} & \frac{v^{(m)}L_{11}^{(m)} - L_7^{(m)}}{R^{(m)}} \end{bmatrix} \begin{bmatrix} x \\ y \\ z \end{bmatrix} = \begin{bmatrix} \frac{L_4^{(1)} - u^{(1)}}{R^{(1)}} \\ \frac{L_8^{(1)} - v^{(1)}}{R^{(1)}} \\ \vdots \\ \frac{L_4^{(m)} - u^{(m)}}{R^{(m)}} \\ \frac{L_8^{(m)} - v^{(m)}}{R^{(m)}} \end{bmatrix} \quad (2.5)$$

, where

$$R^{(m)} = L_9^{(m)} x + L_{10}^{(m)} y + L_{11}^{(m)} z + 1 \quad (2.6)$$

and  $m \geq 2$ .

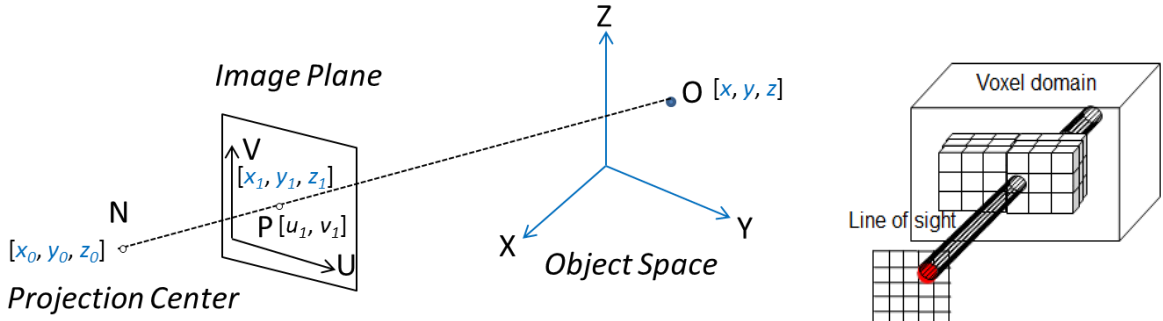


**Fig 2.4** Projection of object space onto image plane

The projection center or the camera position  $N[x_o, y_o, z_o]$  is calculated as

$$\begin{bmatrix} x_0 \\ y_0 \\ z_0 \end{bmatrix} = \begin{bmatrix} L_1 & L_2 & L_3 \\ L_5 & L_6 & L_7 \\ L_9 & L_{10} & L_{11} \end{bmatrix}^{-1} \begin{bmatrix} -L_4 \\ -L_8 \\ -1 \end{bmatrix} \quad (2.7)$$

Given the DLT camera parameter, the 3-D world point  $P[x_k, y_k, z_k]$  correspondent for each pixel position  $[u_k, v_k]$  of the camera as shown in Fig 2.4 is calculated using equation (2.5). And hence the parametric equation of 3D line  $NP$  is calculated as

$$NP = N + (P - N)t$$

$$\begin{bmatrix} x \\ y \\ z \end{bmatrix} = \begin{bmatrix} x_0 \\ y_0 \\ z_0 \end{bmatrix} + \begin{bmatrix} x_n - x_0 \\ y_n - y_0 \\ z_n - z_0 \end{bmatrix} t$$

(2.8)

, where  $t$  is a scalar that varies at each point on the 3D line.

Both the projection center  $N[x_0, y_0, z_0]$  and the equation (2.8) of a 3D line of sight (LOS),  $NP$  passing through a pixel is required for 3D tomographic reconstruction.

## 2.2. Principles of Tomographic-PIV

In tomographic-PIV (Avinash and Malcolm [9]) the scattered light patterns of a test volume, filled with tracer particles and illuminated with a pulsed laser, are recorded simultaneously from several viewing direction using CCD cameras at two subsequent time steps  $t$  and  $t+\Delta t$ . The 3D light intensity distribution over the test volume is reconstructed from its projections on the CCD arrays. Since many different 3D objects can have a single set of projects the problem of reconstruction is a general underdetermined problem. The most likely 3D distribution is described by tomographic principles (Herman and Lent [10]). Once the 3D distribution is known the particle displacement and then velocity within a chosen interrogation volume is obtained by 3D cross-correlation of the reconstructed particle distribution at the two exposures. A combination of 2D cross-correlation in 2D projections instead of a direct 3D cross-correlation over the entire volume is generally used as a best match algorithm for systems with limited resources.

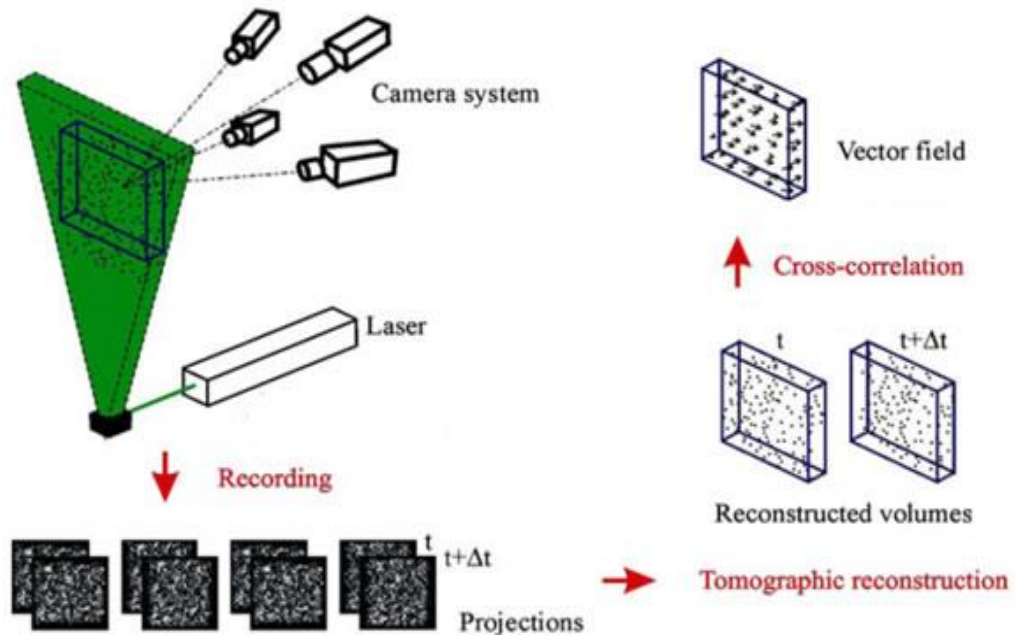


**Fig 2.5** Tomographic-PIV principle (Courtesy: Elsinga [1])

The relation between the world co-ordinate (reconstruction volume) and the image co-ordinate (projections) is established using a calibration model (DLT in this case) as described in section 2.1. The correct tomographic reconstruction of a particle from its images relies on an accurate triangulation of the views from the different cameras, which translates into a calibration accuracy requirement of a fraction of the particle image size.

### 2.3. Tomographic reconstruction algorithm

The particle distribution in images is discretely sampled on pixels from a small number of viewing directions (3 CCD cameras). The images contain high spatial frequencies. Algebraic reconstruction methods (Herman and Lent [10]) are more appropriate than analytical reconstruction methods such as Fourier and back-projection methods for such conditions. These algebraic methods iteratively solve a set of linear equations describing the imaging system.

A measurement volume containing the particle distribution is discretized as a 3D array of cubic voxel elements in  $(X, Y, Z)$  with intensity  $E(X, Y, Z)$ . A cubic voxel element with uniform non-zero value inside and zero outside, with size comparable to that of a pixel is best for the iteration. But the limitation of the execution time and memory requirements limit the size of the cubic voxel element. The projection of a light intensity distribution  $E(X, Y, Z)$  onto an image pixel  $(x_i, y_i)$  returns the pixel intensity  $I(x_i, y_i)$  known from the recorded images, which is expressed as

$$\sum_{j \in N_i} w_{i,j} E(X_j, Y_j, Z_j) = I(x_i, y_i) \quad (2.9)$$

, where  $N_i$  indicates the voxels intercepted or in the neighborhood of the line of sight corresponding to the  $i^{\text{th}}$  pixel  $(x_i, y_i)$  (shaded voxels in Fig 2.6). The weighting coefficient  $w_{i,j}$  describes the contribution of the  $j^{\text{th}}$  voxel with intensity  $E(X, Y, Z)$  to the  $i^{\text{th}}$  pixel intensity  $I(x_i, y_i)$  and is calculated as the intersecting volume between the voxel and the line of sight cylinder, having the cross section area of the pixel, normalized with the voxel volume. The coefficients depend on the relative size of a voxel to a pixel and the distance  $d$  in Fig 2.6 between the voxel center and the line of sight. Weight coefficient  $w_{i,j}$  is between 0 and 1 for all entries  $w_{i,j}$  in the two-dimensional array  $W$  and that  $W$  is very sparse, since a line of sight intersects with only a small part of the total volume.

In Fig 2.6, the top-view of the image plane is shown as a line of pixel elements and the measurement volume is a 2D array of voxels. The gray level indicates the value of the weighing coefficient ( $w_{i,j}$ ) in each of the voxels with respect to the pixel  $I(x_i, y_i)$ .

In the model applying geometrical optics, the recorded pixel intensity is the object intensity  $E(X, Y, Z)$  integrated along the corresponding line of sight. In that case the reconstructed particle is represented by a 3D gaussian-type blob, whose projection in all directions is the diffraction spot. These reconstructed particle blobs are suitable for analysis with existing PIV cross-correlation algorithms providing sub-pixel accuracy.

Finding intensity distribution  $E(X,Y,Z)$  from Equation (2.6) is an underdetermined problem resulting to different solutions. Algebraic reconstruction techniques especially MART (Multiplicative Algebraic Reconstruction Technique (Herman and Lent 1976)) is a well-known reconstruction technique. The false virtual particles as shown by Fig 2.7, manifested from the reconstruction technique are termed as ghost particles. Tomographic-PIV with 3 or more cameras and more robust algorithm is efficient than Algebraic Reconstruction Technique (ART) in reducing the ghost particle count during reconstruction.

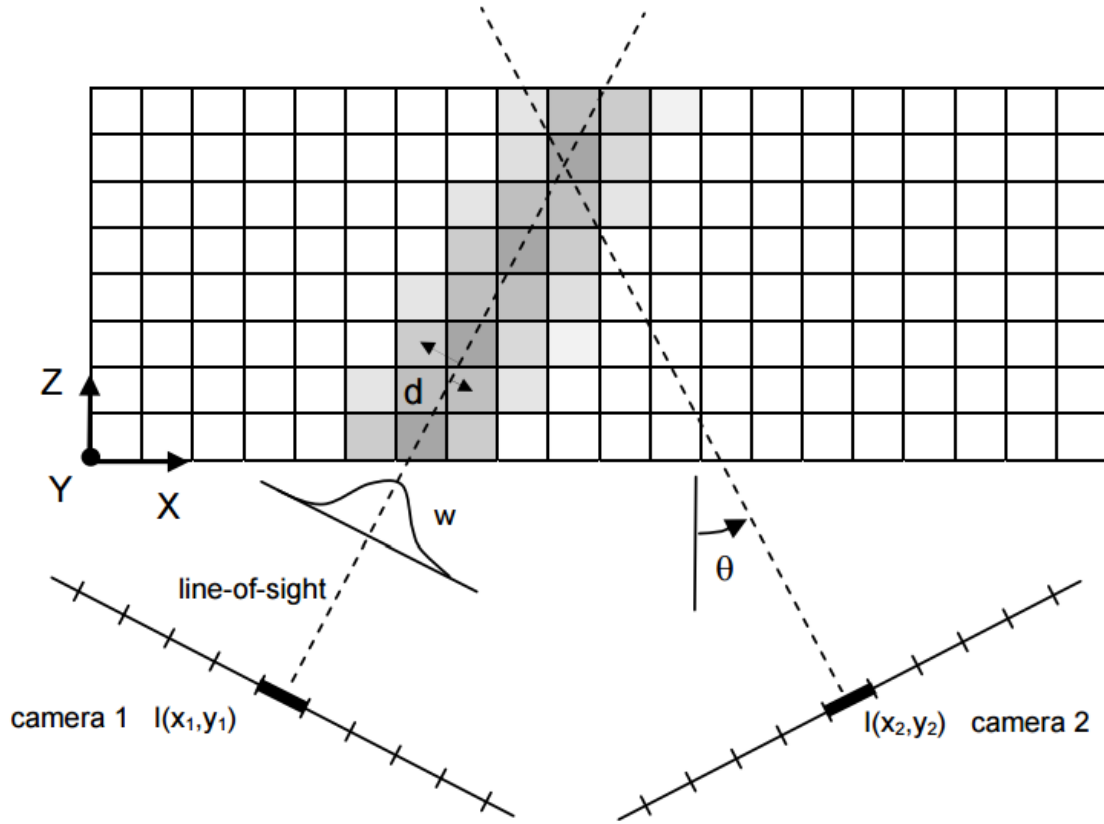


**Fig 2.6** Imaging model used for tomographic reconstruction (Courtesy: Elsinga [1])

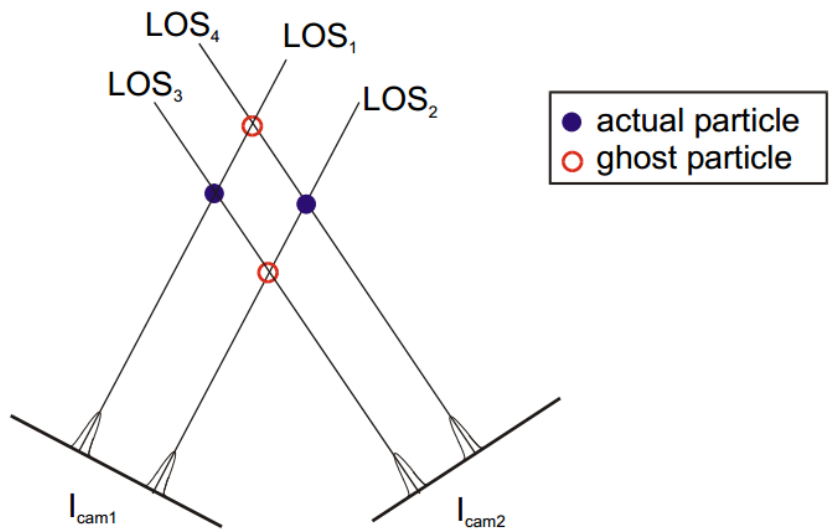


**Fig 2.7** Formation of ghost particles in a 2 camera setup (Courtesy: Elsinga [1])

### 2.3.1. MART

In MART technique (Atkinson and Soria [11]), the intensity distribution of object  $E(X,Y,Z)$  starting from suitable initial guess ( $E(X,Y,Z)^0$  is uniform) is updated in each full iteration as

- 1) for each pixel in each camera  $i$ :
- 2) for each voxel  $j$
- 3) for all voxels along the line of sight

$$E(X_j, Y_j, Z_j)^{k+1} = E(X_j, Y_j, Z_j)^k \left( \frac{I(x_i, y_i)}{\sum_{j \in N_i} w_{i,j} E(X_j, Y_j, Z_j)^k} \right)^{\mu w_{i,j}} \quad (2.10)$$

end loop 3  
end loop 2  
end loop 1

where  $\mu$  is a scalar relaxation parameter which for MART is  $\leq 1$ . The magnitude of the correction is determined by the ratio of the measured pixel intensity  $I$  with the projection of the current object  $\sum_{j \in N_i} w_{i,j} E(X_j, Y_j, Z_j)$ . The exponent ensures that only the elements in  $E(X,Y,Z)$  affecting the  $i^{\text{th}}$  pixel are updated. The MART scheme requires that  $E$  and  $I$  are positive and definite.

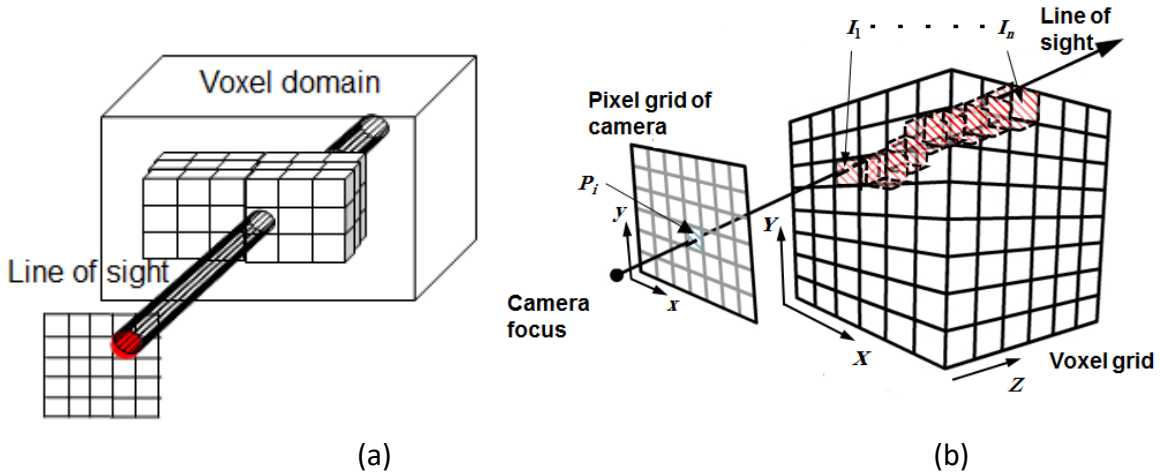


**Fig 2.8** MART reconstruction (a) line of sight projection (b) voxel intensity update

### 2.3.2. Weight Estimation

The weighting coefficient  $w_{i,j}$  that describes the contribution of the  $j^{\text{th}}$  voxel with intensity  $E(X,Y,Z)$  to the pixel intensity  $I(x_i, y_i)$  is calculated as the intersecting volume between the voxel and the line of sight cylinder, having the cross section area of the pixel, normalized with the voxel volume.

A radius  $R$  of a voxel sphere of whose volume is equivalent to a voxel cube of dimension  $L \times B \times H$  is given by

$$R = \sqrt[3]{\frac{3}{4\pi}(LBH)} \quad (2.11)$$

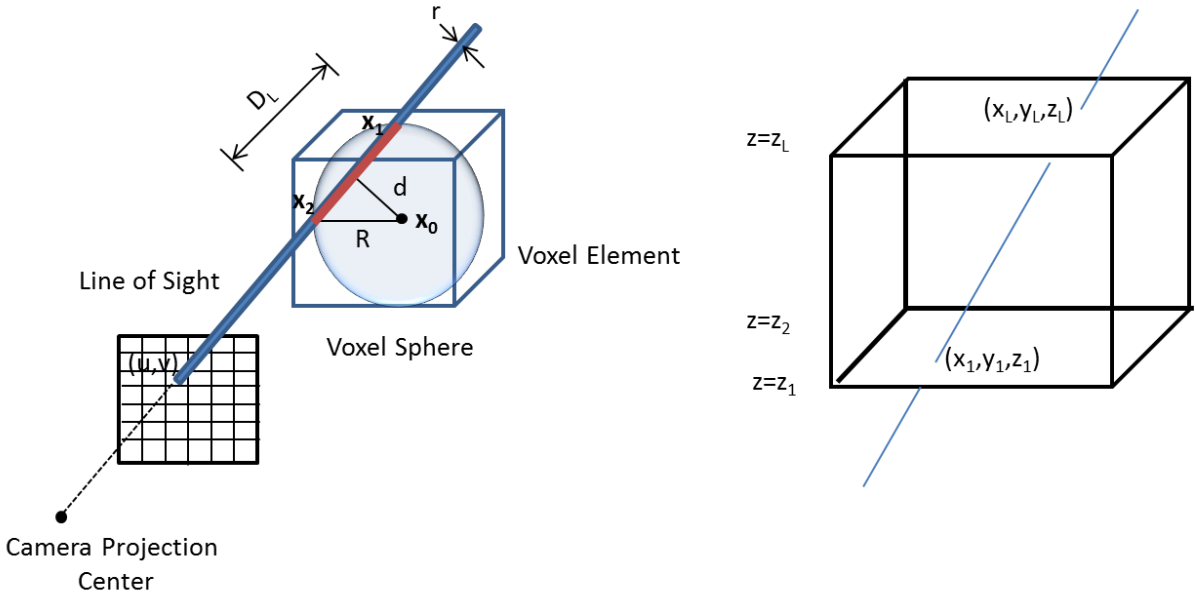


**Fig 2.9** Weight coefficient estimation

And the radius of the line of sight cylinder that has equal area to a physical pixel size of  $L_x \times L_y$  is given by

$$r = \sqrt[2]{\frac{1}{\pi}(L_x L_y)} \quad (2.12)$$

The weight  $w$  is the ratio of the volume of LOS cylinder to the volume of the voxel sphere as given by

$$w = \frac{\pi r^2 D_L}{\frac{4}{3} \pi R^3} \quad (2.13)$$

, where  $D_L$  is the length of the LOS within the intersecting volume shown by red line in Fig 2.9. The length  $D_L$  is calculated from simple Pythagoras theorem as

$$D_L = 2\sqrt{R^2 - d^2} \quad (2.14)$$

, where  $d$  is the distance from the center of the voxel sphere  $x_0$  to the 3D line of sight given by equation (2.15) passing through the camera projection center and the pixel co-ordinate  $(u, v)$ . The world position of the camera projection center and the pixel co-ordinate  $(u, v)$  are found using the calibration model. The distance from the voxel center  $x_0$  to 3D-LOS intersecting the voxel sphere at two positions  $x_1$  and  $x_2$  is given by

$$d = \frac{\left| (\vec{x}_2 - \vec{x}_1) \times (\vec{x}_1 - \vec{x}_0) \right|}{\left| (\vec{x}_2 - \vec{x}_1) \right|} \quad (2.15)$$

For the 3D LOS intersecting any plane of reconstruction at  $z = z_1$ , the parametric constant for the 3D line is calculated as

$$t = \frac{(z - z_1)}{dz} \quad (2.16)$$

$dz$  is the reconstruction resolution in  $z$  direction which is fixed. So for a point with  $z$  coordinate, the other  $x$  and  $y$  co-ordinates are calculated from equation (2.8).

## 2.4. Displacement vector

Displacement vector in PIV analysis is done using 2D cross-correlation (Bilsky et. al. [12]) between images for 2D velocity profile and between voxels for 3D velocity profiles. Basically for a 2D velocity profile, a pair of images is divided into smaller regions (interrogation windows). The cross-correlation between these images of sub-regions measures the optical flow (displacement or velocity of the objects) within the image pair. By progressively decreasing the interrogation windows size, a better PIV resolution can be achieved. The 2D cross correlation between two images is defined as

$$r(x, y) = \frac{\sum_x \sum_y (p(x, y) - \bar{p})(q(x + \Delta x, y + \Delta y) - \bar{q})}{\sqrt{\sum_x \sum_y (p(x, y) - \bar{p})^2} \sqrt{\sum_x \sum_y (q(x + \Delta x, y + \Delta y) - \bar{q})^2}} \quad (2.17)$$

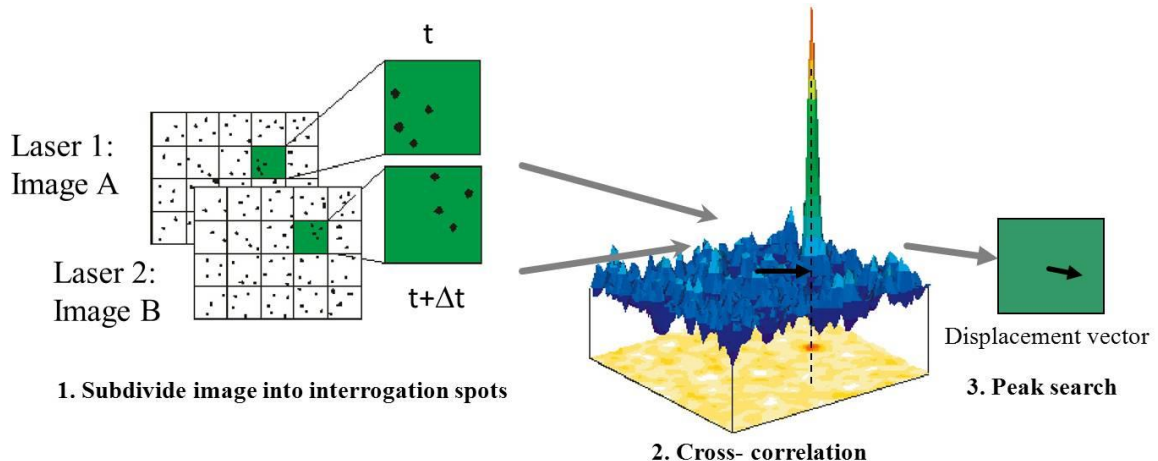


**Fig 2.10** Cross correlation analysis using template matching method (Courtesy: LAVISION)

The displacement vector is calculated using the template matching method with normalized correlation coefficient algorithm as described by equation (2.17), where the interrogation window is compared against a larger searching window. For a given sub-section of Image A (taken at time  $t$ ), the sub-section of Image B (taken at time  $t + \Delta t$ ) that best matches (highest cross correlation coefficient) is considered as the displacement which is depicted in Fig 2.10. The notion of 2-D cross correlation can be further extended into 3-D which involves searching for a sub-voxel region at time  $t + \Delta t$  that best matches a given sub-voxel region at time  $t$  to find the three component of the displacement. The 3-D cross correlation between two voxels is defined as

$$r(x, y, z) = \frac{\sum_{x} \sum_{y} \sum_{z} (p(x, y, z) - \bar{p})(q(x + \Delta x, y + \Delta y, z + \Delta z) - \bar{q})}{\sqrt{\sum_{x} \sum_{y} \sum_{z} (p(x, y, z) - \bar{p})^2} \sqrt{\sum_{x} \sum_{y} \sum_{z} (q(x + \Delta x, y + \Delta y, z + \Delta z) - \bar{q})^2}} \quad (2.18)$$

Equation (2.18) represents a direct 3-D cross correlation algorithm which is expensive in both memory and execution time. For limited memory resources and relatively faster execution an indirect method of 2-D cross correlation in each orthogonal plane is performed to calculate separate components displacement vector as shown in Fig 2.11. This is called parallel projection correlation (PPC).

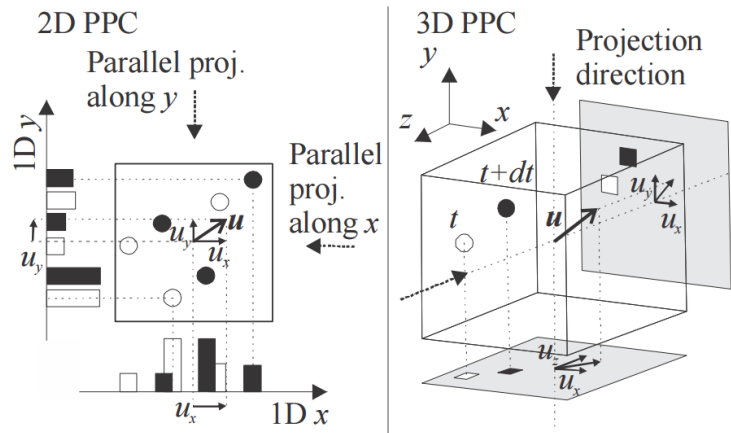


**Fig 2.11** Parallel projection correlation (Courtesy: BILSKY [12])

At the first step, two parallel projections of every interrogation sub-volume of the full reconstructed volume image are calculated. Then each parallel projection pair (for  $t, t + \Delta t$  time steps) of a sub-volume along x, y or z directions is cross-correlated. The location of the highest correlation maximum for each 2D correlation function separately gives two of the three required displacement components. For example  $v_x$  and  $v_y$  displacement components are obtained from the projection along z-axis. Doing the same along y-axis  $v_x$  and  $v_z$  can be obtained. Thus only two 2D parallel projection correlations (PPC) are sufficient to get a 3D displacement vector which saves both memory and execution time.

Once the displacement vector is determined, it can be converted to flow velocity  $v$  using the time separation between laser shots  $\Delta t$  and the displacement vector  $X$  as described by

$$\vec{v} = \frac{\vec{X}}{M\Delta t} \quad (2.19)$$

, where  $M$  is the object/image magnification factor.

## 2.5. Flow velocity and vorticity

Flow velocity in fluid dynamics is a vector field which is used to mathematically describe the motion of a continuum. It is the rate of change of position  $dr$  per unit time  $dt$ . The length of the flow velocity vector is the flow speed and is a scalar. In mathematical terms, the velocity of a fluid is the derivative of the position vector of a fluid with respect to time given by equation (2.20). As a vector quantity, fluid velocity must have at least one non-zero directional component and may have up to three non-zero directional components. The velocity vector has non-zero components in any orthogonal direction along which motion of the fluid occurs.

$$\vec{v} = \frac{\vec{dr}}{dt} \rightarrow \vec{v} = \left\langle \frac{dr_x}{dt}, \frac{dr_y}{dt}, \frac{dr_z}{dt} \right\rangle \quad (2.20)$$

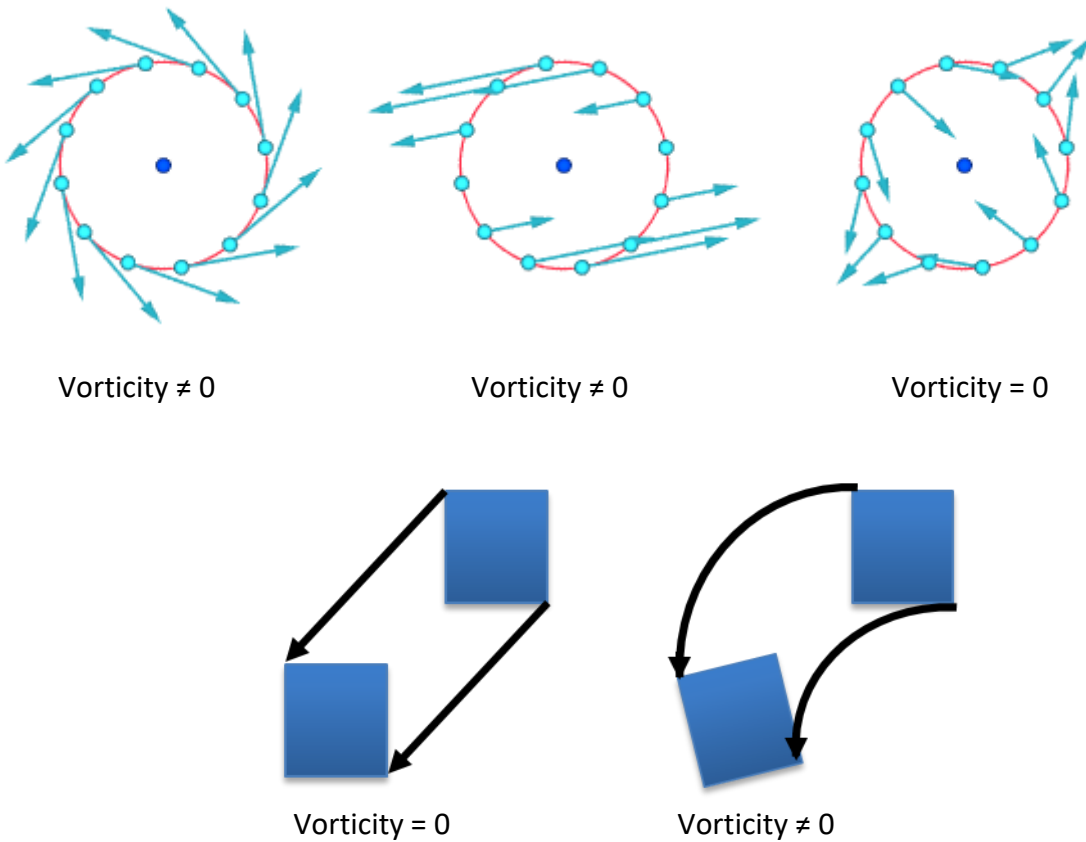


**Fig 2.12** Examples of some zero and non-zero vorticity

Flow vorticity is a pseudo-vector field that describes the local spinning motion of a continuum near some point (the tendency of something to rotate), as would be seen by an

observer at that point and travelling along with the flow. Fig 2.12 shows some of the cases for zero and non-zero vorticity cases. Simply the vorticity is non-zero when a tiny part of the continuum has rotation rather than just moving with the flow. Mathematically, the vorticity of a three-dimensional flow is defined as the curl of the velocity field  $v$  described as

$$\begin{aligned}\vec{\omega} &= \nabla \times \vec{v} = \left( \frac{\partial}{\partial x}, \frac{\partial}{\partial y}, \frac{\partial}{\partial z} \right) \times (v_x, v_y, v_z) \\ \vec{\omega} &= \left( \frac{\partial v_z}{\partial y} - \frac{\partial v_y}{\partial z}, \frac{\partial v_x}{\partial z} - \frac{\partial v_z}{\partial x}, \frac{\partial v_y}{\partial x} - \frac{\partial v_x}{\partial y} \right)\end{aligned}\quad (2.21)$$

The vorticity tells how the velocity vector changes when one moves by an infinitesimal distance in a direction perpendicular to it. Vorticity allows one to form a powerful qualitative description for the formation and separation of boundary layers in the fluid flow dynamics.

## 2.6. Gaussian mask cross correlation (GMCC)

The Gaussian filter is a 2-D convolution operator that uses 2D Gaussian distribution as a point-spread function. Mathematically the 2D gaussian distribution, as shown in Fig 2.13, is described as

$$G(x, y) = \frac{1}{2\pi\sigma^2} e^{-\frac{x^2+y^2}{2\sigma^2}} \quad (2.22)$$

, where  $\sigma$  represents the standard deviation of two dimensional distribution in  $x$  and  $y$ .  $\sigma$  relates to the diameter of the particle to be detected.

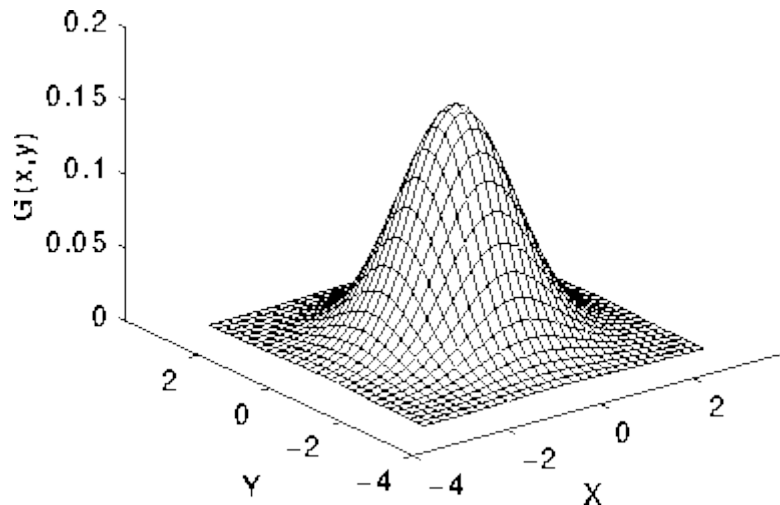


**Fig 2.13** 2D gaussian distribution with mean (0, 0) and  $\sigma=1.0$

Any dot that highly matches the point-spread function as shown in Fig 2.14(a) is extracted from an image by using this kernel. An example of a 2D gaussian kernel with  $\sigma = 1.0$  and mask size of  $5 \times 5$  is shown in Fig 2.14(b). The value 273 is the sum of all the values in the

mask. The value of the mask size varies according to the particle that is to be detected. The Gaussian mask is convoluted over the entire image to detect any particles in the image. In case of a detected particle, the correlation value is greater than the correlation threshold value set in the algorithm. With gaussian mask cross correlation, the location of the particle is detected within an accuracy of 10<sup>th</sup> of a pixel.

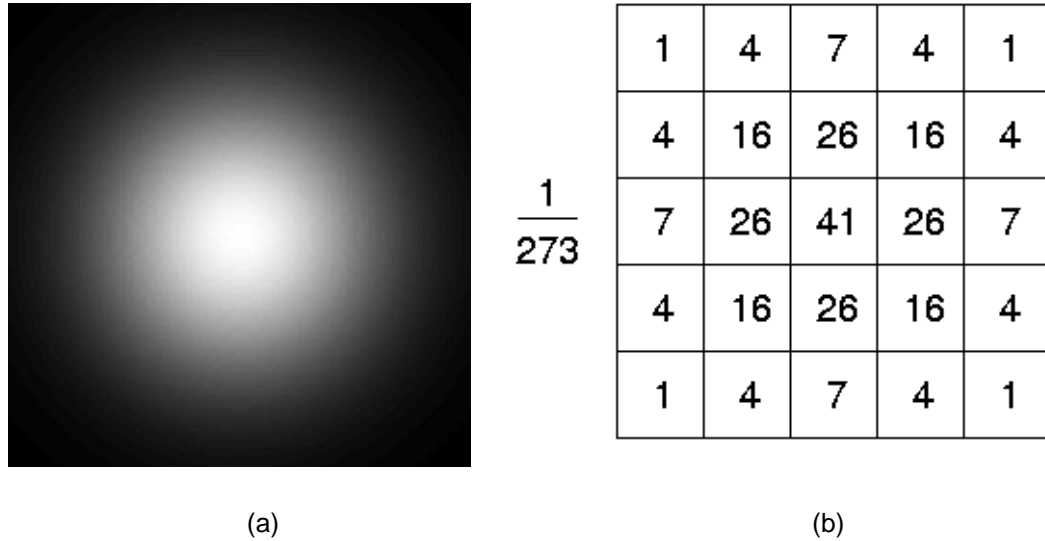


**Fig 2.14** Gaussian distribution (a) point-spread function (b) kernel or mask

## 2.7. Sub-Pixel Estimation

Sub-pixel estimation is the process of estimating the value of a geometric quantity to better than pixel accuracy (Nobach [13]), even though the data was originally sampled on an integer pixel quantized space. Among various approaches a simple approach to estimate the sub-pixel position is the interpolation. A three point gaussian estimator in a one dimensional is defined as

$$G(x) = \frac{1}{2\pi\sigma^2} e^{-\frac{(x-x_c)^2}{2\sigma^2}} \quad (2.23)$$

, where  $G(x)$  is a one-dimensional gaussian distribution in variable  $x$  with mean  $x_c$  and standard deviation  $\sigma$ .

The mean  $x_c$  in sub-pixel accuracy can be found as a 3 point Gaussian fit given by

$$x_c = x_0 + \frac{\ln G_{0-1} - \ln G_{0+1}}{2(\ln G_{0-1} + \ln G_{0+1} - 2\ln G_0)} \quad (2.24)$$

The same equation is used for finding  $y_c$ , therefore five points are needed to estimate the  $x$  and  $y$  location of a particle with sub-pixel accuracy as shown in Fig 2.15. The diameter of the particle to be detected is directly related to the variance

$$\sigma^2 = \frac{\ln G_{0+1} - \ln G_0}{(x_0 - x_c)^2 - (x_{0+1} - x_c)^2} \quad (2.25)$$

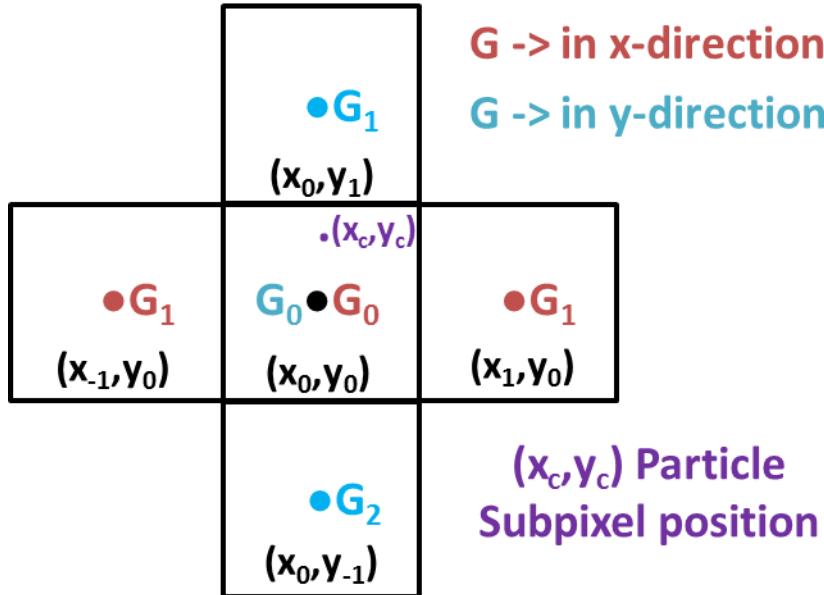


**Fig 2.15** Three-point gaussian fit for sub-pixel estimation

The location of the particle measured at an accuracy of 10<sup>th</sup> of pixel from GMCC is further interpolated by 3 point Gaussian fit to obtain a further sub-pixel accuracy of 1000<sup>th</sup> of a pixel.

## 3. Research Methodology

### 3.1. Experimental setup

As a laboratory model of a close water area, regular octagonal water tank has been employed after reference study of Hanari and Sakakibara [13]. This tank is made of transparent acrylic glass of side length 352 mm (805 mm distance between two parallel sides 915 mm distance between diagonal corners) and 1000 mm in height which is filled up with water up to 950 mm. The impeller for rising current generation is 1/20<sup>th</sup> scale of the real model and is installed at 30 to 60 mm depth from the water surface in the center of the water tank and is driven by a DC servo motor (Oriental Motor Co. Ltd.: BLHM450K-A) situated above water. The impeller and the motor are connected by a vertical axis but separated by a thin (3 mm thick) transparent plate, which covers the entire surface of the water surface and works as a surface wave canceller. Figure 3.1 is a schematic diagram of the layout of this water tank with a submerged two-step impeller. The upper and lower impellers are both 50 mm in outer diameter, 6 mm in axial thickness and have four vanes in circumferential direction. The planar vanes of the lower impeller are incident at 45°, while those of the upper impeller are at 90°. In addition, the four vanes of the upper and lower impellers are placed with a staggered angle of 45°. The inclined lower vanes and vertical upper vanes of the impeller were designed to optimize the maximum extraction.

For the 3D tomographic PIV experiment, a fine chemical particle (Mitsubishi Chemical: Sepabeads SP2MGS) of about 120  $\mu\text{m}$  average diameter is used to observe the tornado-like rising current caused due to the swirling of water inside the water tank by the immersed impeller. A laser light sheet of about 20 mm thickness at the middle height horizontal cross section of the experimental water tank was used to illuminate the seed particles during the experiment. A pulse generator (112 Hz) was used as a master synchronizing trigger pulse which was then used to trigger the three viewing cameras externally. The master trigger pulse was divided down to 14 Hz with some delay in order to drive the laser unit. The images (1280 x 1024 resolutions) of the illuminated section were taken by the three cameras and the images were stored in a PC.

The behavior of water tornado rise in a PCS was observed and then investigated using tomographic PIV and the effects of different parameters were analyzed by varying

- Immersed depth to water tank height ratio,  $d/H = 0.03-0.06$
- Motor rotation speed from 1000-2200 rotation per minute (rpm)

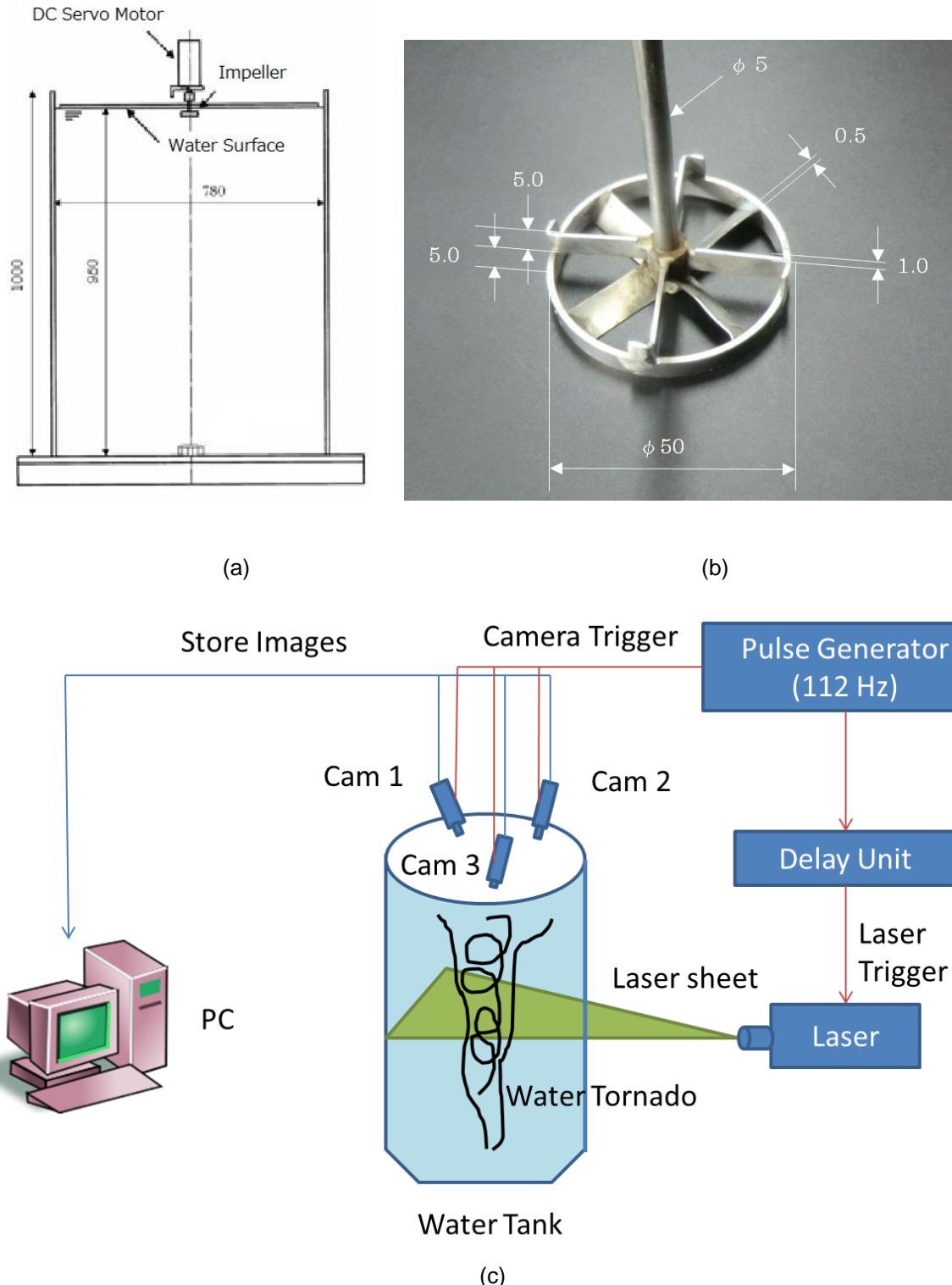


**Fig 3.1** Schematics of experimental setup  
 (a) Water Tank side view (b) Rotary Impeller (c) Overview system diagram

### 3.2. Calibration Procedure

Direct Linear Transformation (DLT) algorithm as described in section 2.1.2 was used for camera calibration process. A 3-D calibration plate with three depth levels at 2 mm spacing

and 120 known control points with 10 mm vertical and horizontal spacing as shown in Fig 3.2 was used. The images of calibration plate were as shown in Fig 3.3 were taken from three viewing cameras prior to the PIV experiment.

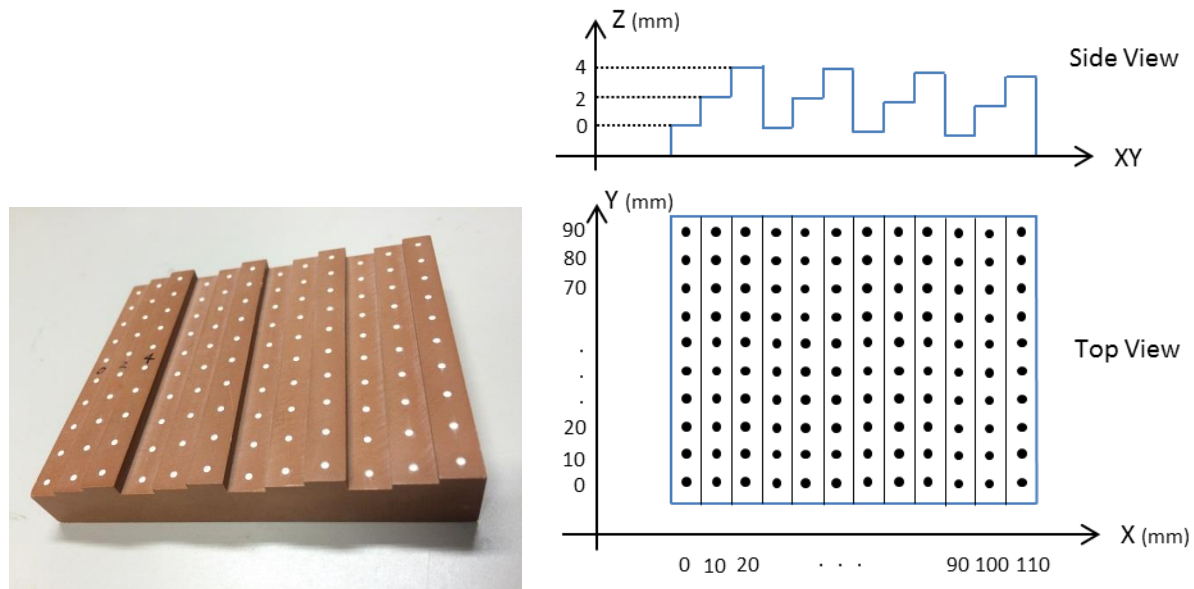


**Fig 3.2** Calibration Plate (a) real 3D view (b) top and side view with physical dimensions

The centroid of calibration dots in each calibration image was detected using Gaussian Mask Cross Correlation (GMCC) binarization method with following parameters

- Mask-size = 11px
- Particle diameter(in image) = 11px
- Cross-correlation threshold = 0.6-0.8

Orderly detection of every dot using the binarization method was manually verified in excel file. One of the verified snap-shot is shown in Fig 3.4.



**Fig 3.3** Raw images of calibration plate taken from three viewing cameras

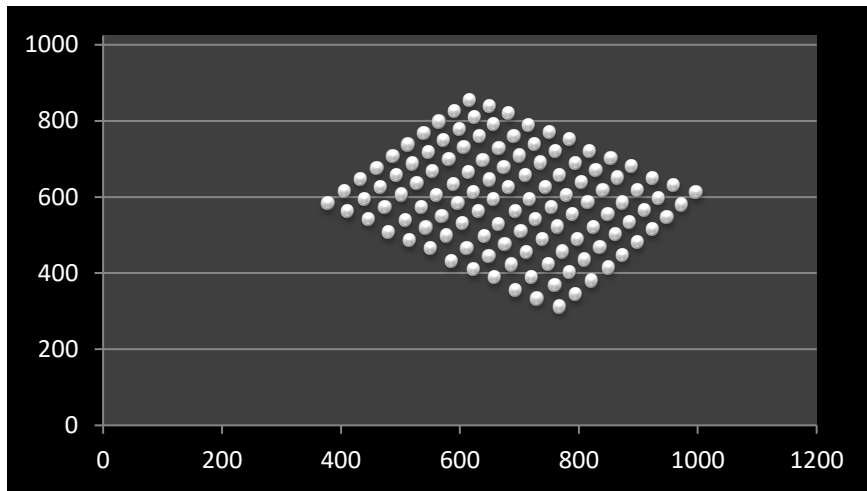


**Fig 3.4** Excel verification of detection of dot-order for one of the calibration image

### 3.3. Experiment parameters

The following Table 3.1 to Table 3.5 lists various experimental and algorithmic parameters used for 3D tomographic reconstruction and cross-correlation procedures.

**Table 3.1** Camera Specifications

<b>Camera</b>	IDT: X-Stream XS-3
<b>Image Resolution</b>	1280H x 1024V (H->Horizontal , V-> Vertical)
<b>Pixel Depth</b>	8 bits
<b>Max Frame Rate</b>	614 Hz @ 1280H x 1024V (up to 1280H x 10V @ 57,239 Hz)
<b>Pixel Size</b>	12 x 12 micron

Raw images (8-bit grayscale, 1280H x 1024V resolution) were captured using a high speed camera (IDT: X-Stream XS-3). The cameras have internal memory so that during the experiment all images are stored in the cameras without the involvement of storing PC. Later the images are saved back to storing PC. This ensures that all three images are taken at the same time-instant without any delay contributed by PC.

**Table 3.2** Experiment parameters

<b>No of Camera</b>	3
<b>Camera Frame Rate</b>	112 Hz (~8.03 ms)
<b>Laser Sheet Thickness</b>	20 mm
<b>Laser</b>	ND-YAG Pulse Laser (532 nm)
<b>Seed</b>	120 $\mu\text{m}$ average diameter

The ND-YAG Pulse laser (532 nm) was turned into a light using a cylindrical lens. This lens was configured to illuminate the 20 mm thickness volume of a tornado cross section filled with PIV particle seeds of approximately 120  $\mu\text{m}$  average diameter. The image of the scene was captured by three different viewing cameras located above the tank.

**Table 3.3** Calibration parameters

<b>Calibration plate</b>	3D type
<b>Number of dots</b>	120
<b>Particle detection</b>	GMCC (mask size = 11, particle diameter = 11, cross-correlation threshold = 0.6~0.8)
<b>Sub-pixel accuracy</b>	YES

A 3D calibration plate with total of 120 dots as shown in Fig 3.2 was used in the calibration procedure. The GMCC and then 3-point gaussian fit was used to detect the dot centroid with sub-pixel accuracy.

**Table 3.4** Reconstruction parameters

<b>Iteration number</b>	30
<b>Relaxation Parameter</b>	1.0
<b>Reconstruction Volume</b>	168 x 168 x 16 mm <sup>3</sup>
<b>No of Voxels</b>	560 x 560 x 80
<b>Single Voxel Size</b>	0.3 x 0.3 x 0.2 mm <sup>3</sup>
<b>Reconstruction Type</b>	3D-3C

For the tomography analysis, the interrogation test volume of 168 x 168 x 16 mm<sup>3</sup> was divided into 560 x 560 x 80 voxels, the size of a single voxel being 0.3 x 0.3 x 0.2 mm<sup>3</sup>. Each voxel is assumed to have uniform intensity. This is equivalent to image discretization process. The voxel is considered to include a particle if it has non-zero intensity. Tomographic reconstruction with relaxation parameter 1.0 was used to detect the position of the particle in the 3-D volume.

**Table 3.5** Correlation parameters

<b>Correlation Mask Size</b>	32 x 32 x 16
<b>Vector Interval</b>	8 x 8 x 8

After the 3-D position of the particles for two consecutive time steps have been calculated, the displacement vector was calculated using a cross-correlation. A mask size of 32 x 32 x 16 was used for 3D cross correlation to find the displacement vectors across the entire volume at an interval of 8 voxels in each x, y and z-direction.

## 4. Results and Discussions

### 4.1. Calibration Accuracy

The detection of the centroid of every dot in calibration procedure was obtained to 10<sup>th</sup> of a pixel using GMCC and 1000<sup>th</sup> of a pixel using sub-pixel accuracy. Mapping the 3D world coordinate of the calibration dots to the corresponding image coordinates in the subsequent calibration images and then applying the DLT algorithm, the maximum calibration error was determined to be less than 1.2mm for 3D reconstruction of the dots from the calibration images as shown in Fig 4.1.

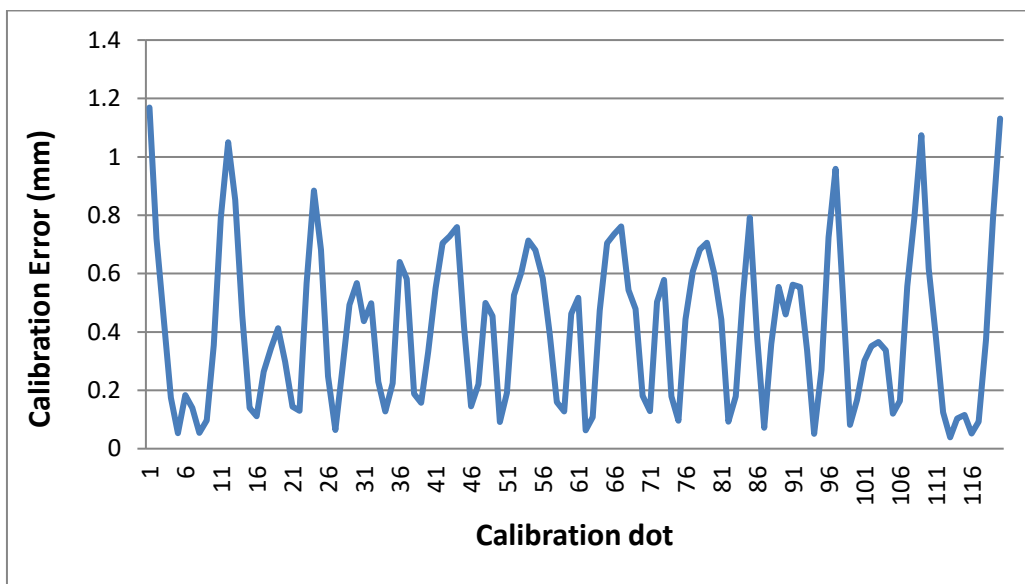


**Fig 4.1** Calibration error

### 4.2. Raw Images

Fig 4.2 shows the raw images of the projection of a 3D scene of a tornado flow taken by three different viewing cameras at 112 Hz frame rate and 1280H x 1024V resolution. Since the cameras are located above the tank as shown in Fig 3.1, the cameras capture a cross-section of a specific width of a tornado flow development. For the tornado flow rise analysis, the cameras capture the entire circulating vortex and the periphery around it which gives both the qualitative and quantitative measurement of the tornado flow development. The images in their raw format without any image post-processing were used for further analysis.

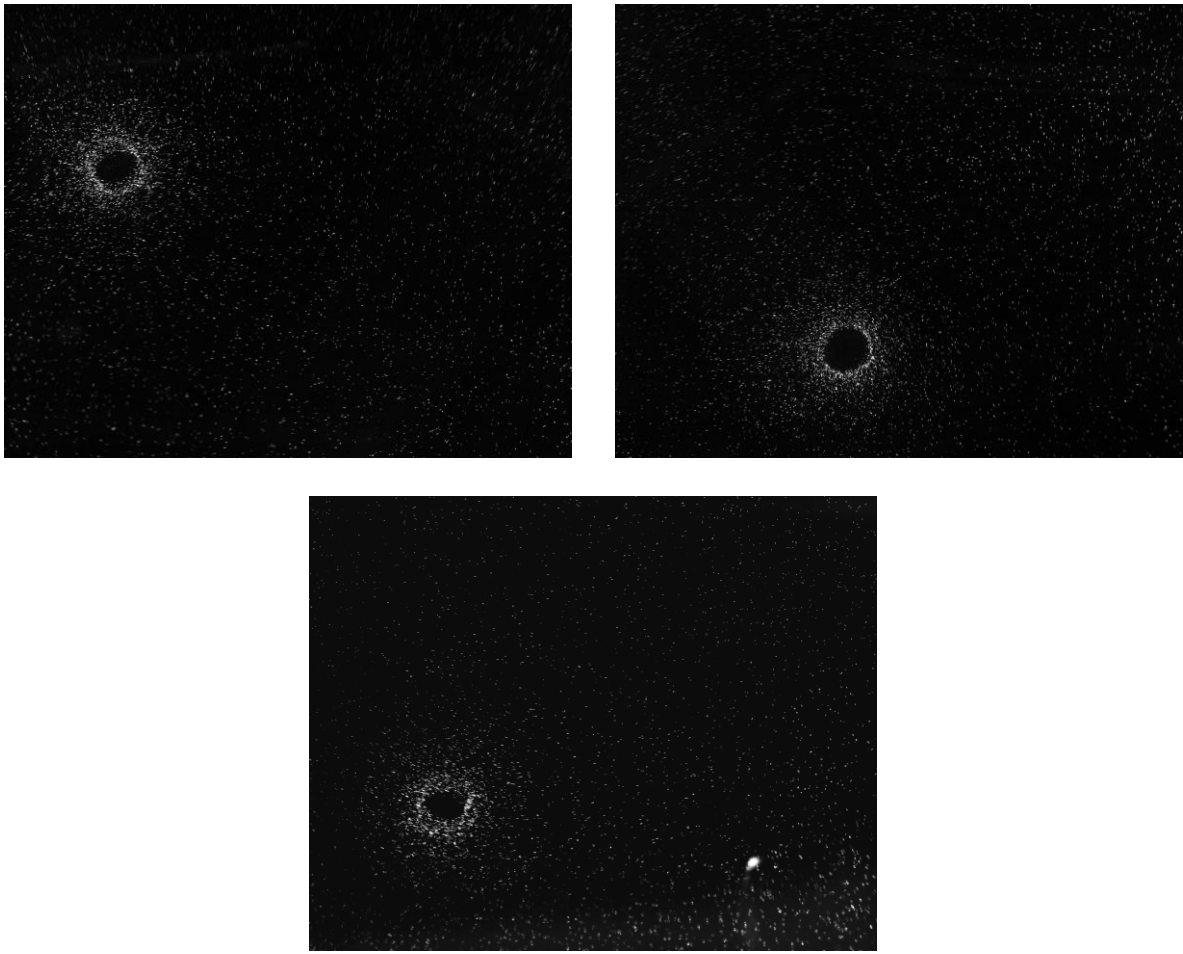
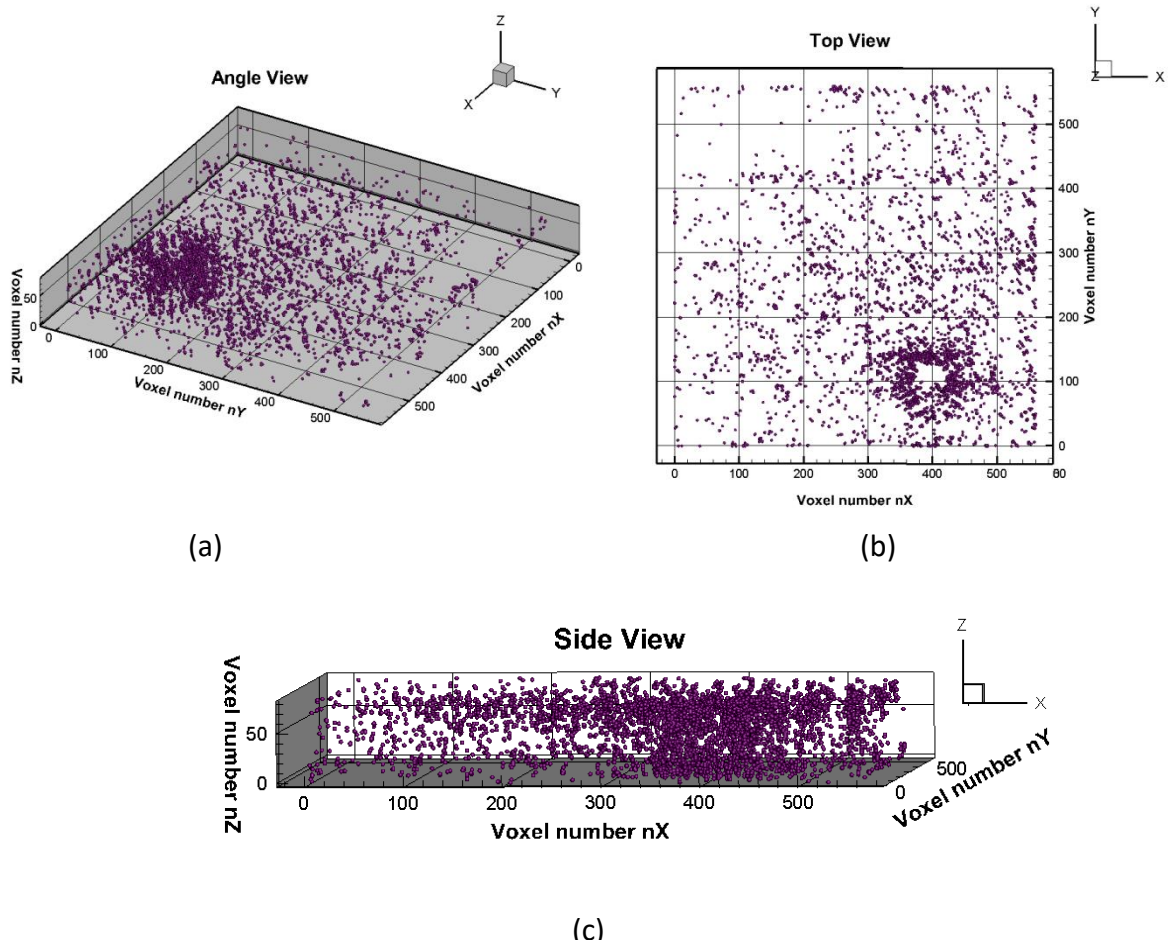


**Fig 4.2** Raw image of tornado flow taken from three different viewing cameras

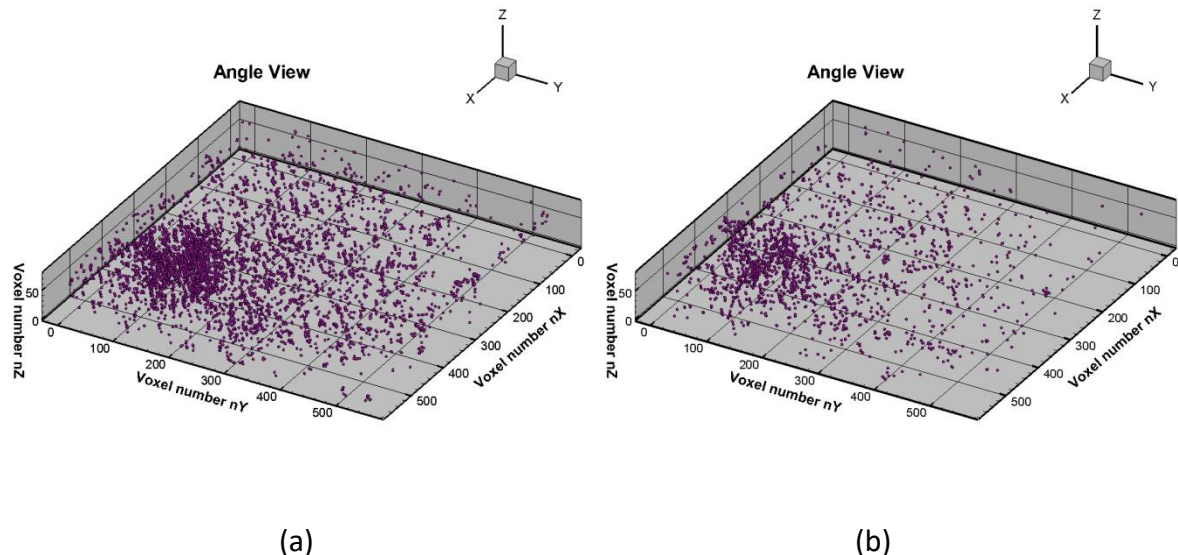
### 4.3. Voxel (Positional) reconstructions

Fig 4.3 shows the angle, top and side view of the voxel or positional reconstruction of raw images of Fig 4.2. The 3D position of particles in the 3D volume was reconstructed using MART algorithm as described in section 2.3. The tornado-like rising flow at full development stage is characterized by highly concentrated seed particles along the outer edge of the rotating water tornado. This is most probably due to the centrifugal force induced by the enforced rotating flow as well as due to the strong velocity gradient along the circumferential part of the water tornado. By contrast, the tornado flow at post breakdown stage is characterized by rather dispersed seed particles along the edge of the rotating water tornado. Not only that, the seed particles at this stage are found less actively distributed around the water tornado probably because of the attenuated rotating motion.

The 3D reconstruction ranges were needed to be adjusted in every experiment to have a nice tornado-view at the center of the reconstructed volume. But the ranges were kept constant for different time steps of the same experiment to verify the movement of the tornado.



**Fig 4.3** Voxel (3D positional) reconstruction (a) angle view (b) top view (c) side view



**Fig 4.4** Tomographic reconstructions at different stages  
(a) full development (b) post breakdown

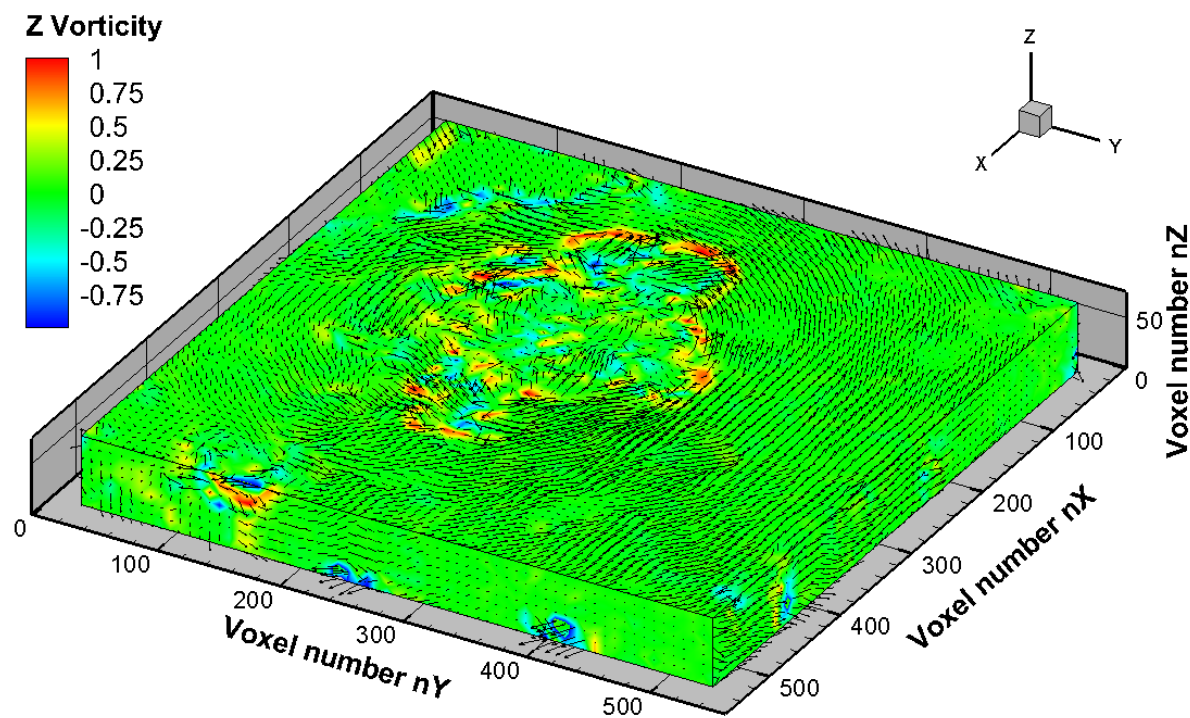
## 4.4. Velocity reconstructions

Various velocity reconstructions within the entire test volume and slices of the volume are presented below. The temporal characteristics of the tornado-flow rise and the behavior of the tornado flow rise at different cross sectional heights, motor speed and impeller immersed depth is also presented.

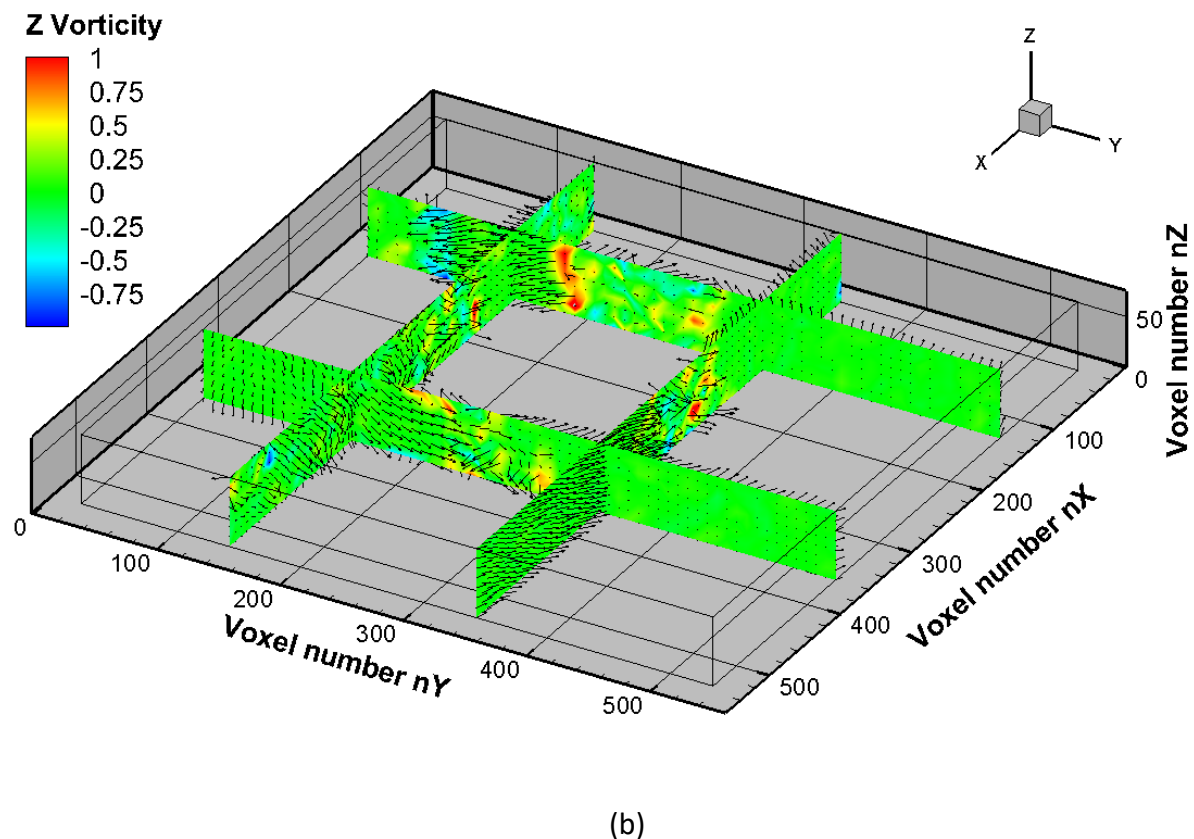
### 4.4.1. 3D-3C Reconstruction

Fig 4.5(a) shows the 3D-3C velocity reconstruction of the investigated volume of  $168 \times 168 \times 16$  mm<sup>3</sup> divided into discretized total 3D voxels of  $560 \times 560 \times 80$  count, providing the vectors at intervals of 0.3, 0.3 and 0.2 mm in x, y and z direction respectively. The instantaneous PIV results were calculated from two consecutive time steps result of tomographic reconstructions of the tornado-like rising flow at full development stage. The 3C vector (black arrows) in a 3D position represents the velocity of the flow at that location and the colors from blue (max negative vorticity) to red (max positive vorticity) represents the contours of the z-component of the vorticity.

Fig 4.5(b) shows the vertical cross-sections in x and y direction of the investigated volume across the tornado boundary which clearly depicts the counter clock-wise swirl of the tornado-flow at a given height of the tornado. It also shows similar nature of tornado flow rise at every cross-sectional height of the tornado. Most of the surrounding part (green) does not have any swirling motion and contribute little towards any undesirable mix of the sediments to the neighborhood. Very small tornado rising and falling can be seen outside the tornado boundary that contributes very little towards the surrounding mix.



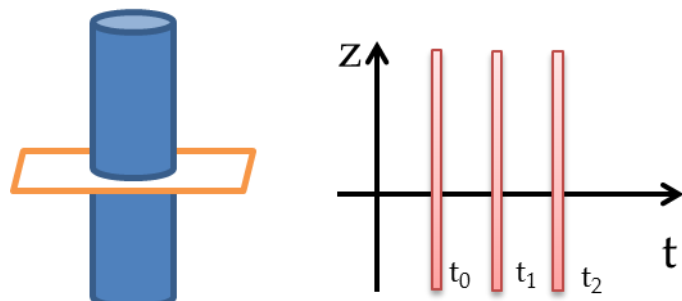
(a)



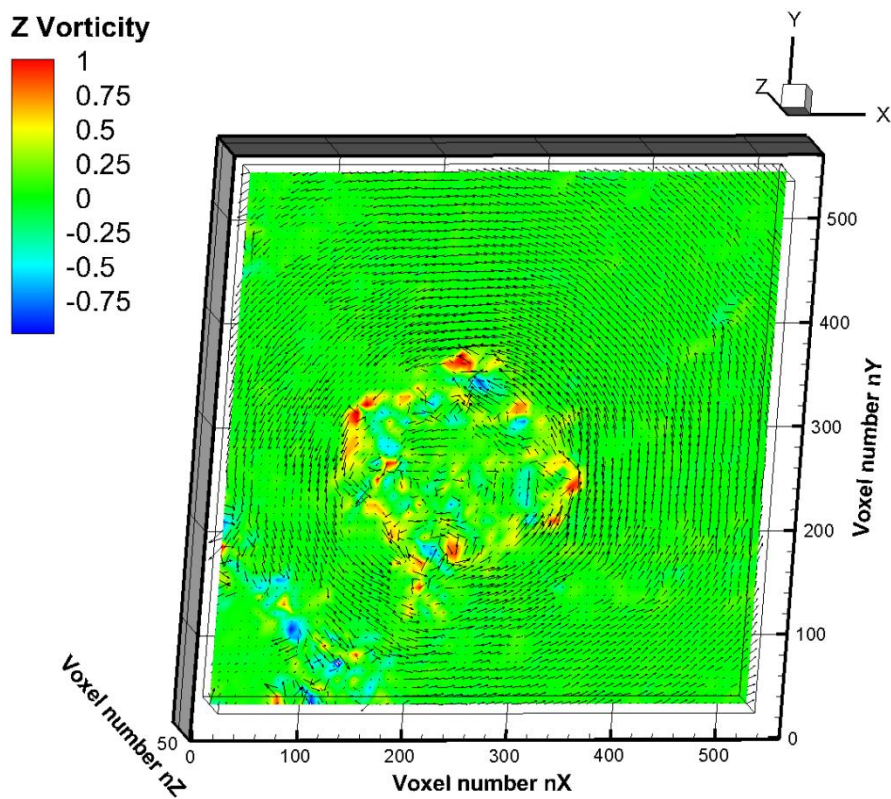
**Fig 4.5** 3-D 3C displacement reconstruction (a) vorticity contours color coded with z-component (b) X and Y planar cross-sections of the boundaries of the tornado

A highly increased circumferential velocity area (red ring) with high vorticity forms the outer edge of the rotating water tornado. Also an inner ring (blue) of low vorticity having opposite swirling motion can also be seen. These contribute to the fact that the local volume around the tornado boundary fall into the tornado flow rising in two different swirling actions: one rising outside the tornado boundary and the other falling inside the tornado boundary. The prominent ring (red) of high vorticity is clearly seen to be extending from top to bottom height of the tornado which means the tornado-rise is consistent over the entire investigated volume.

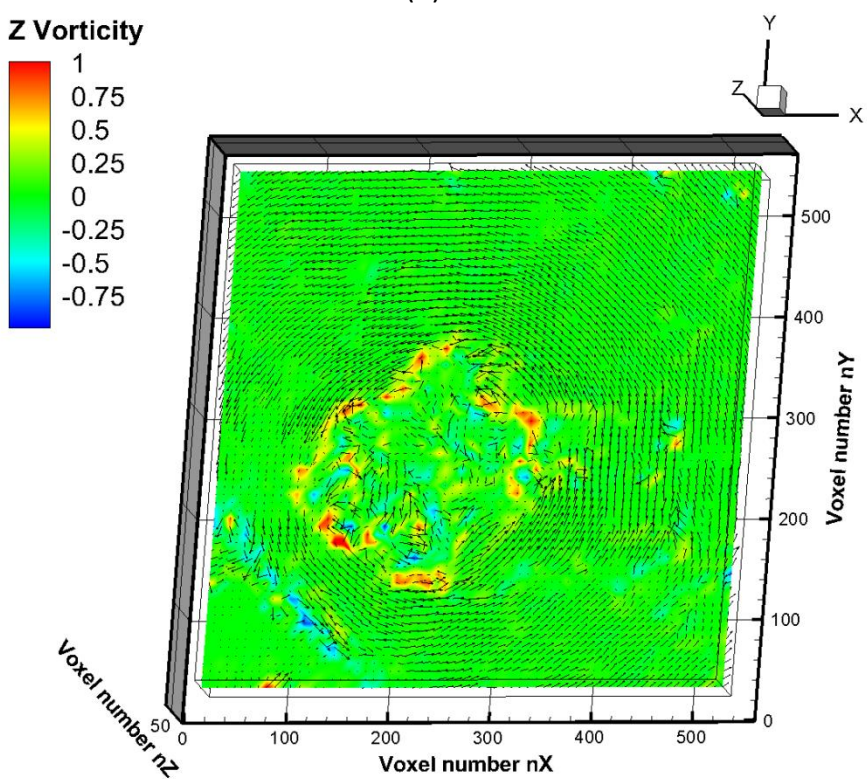
#### 4.4.2. Tornado flow temporal characteristics at a fixed height



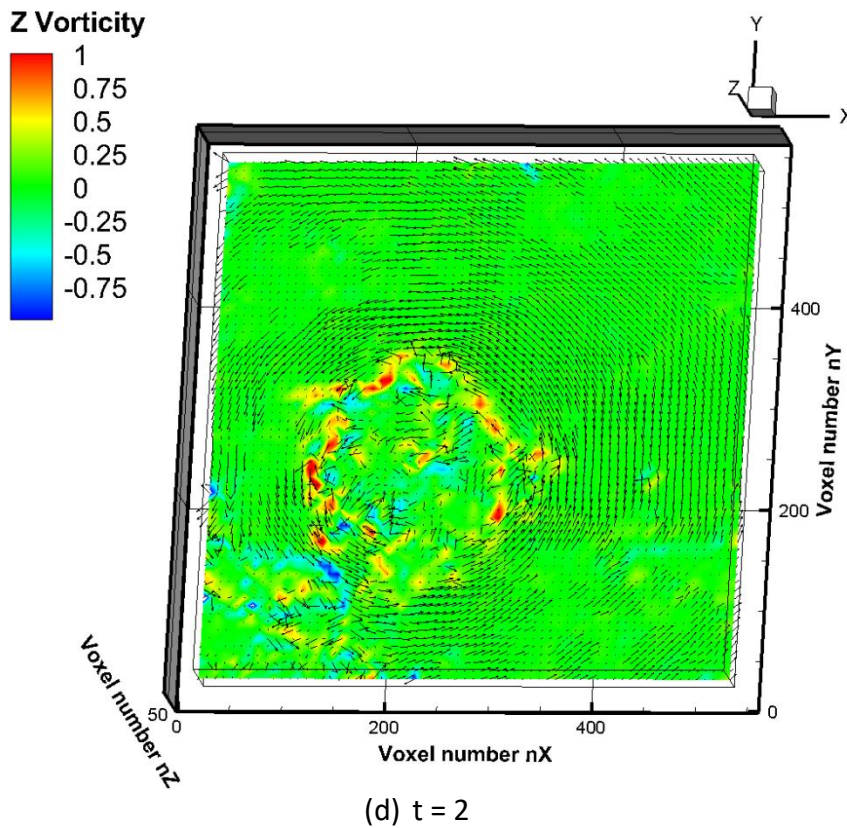
(a) Conceptual Schematic



(b)  $t = 0$



(c)  $t = 1$

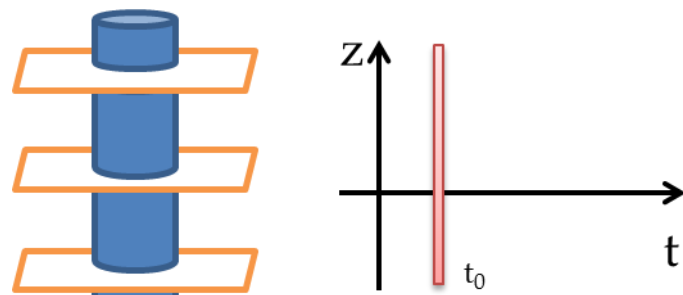


(d)  $t = 2$

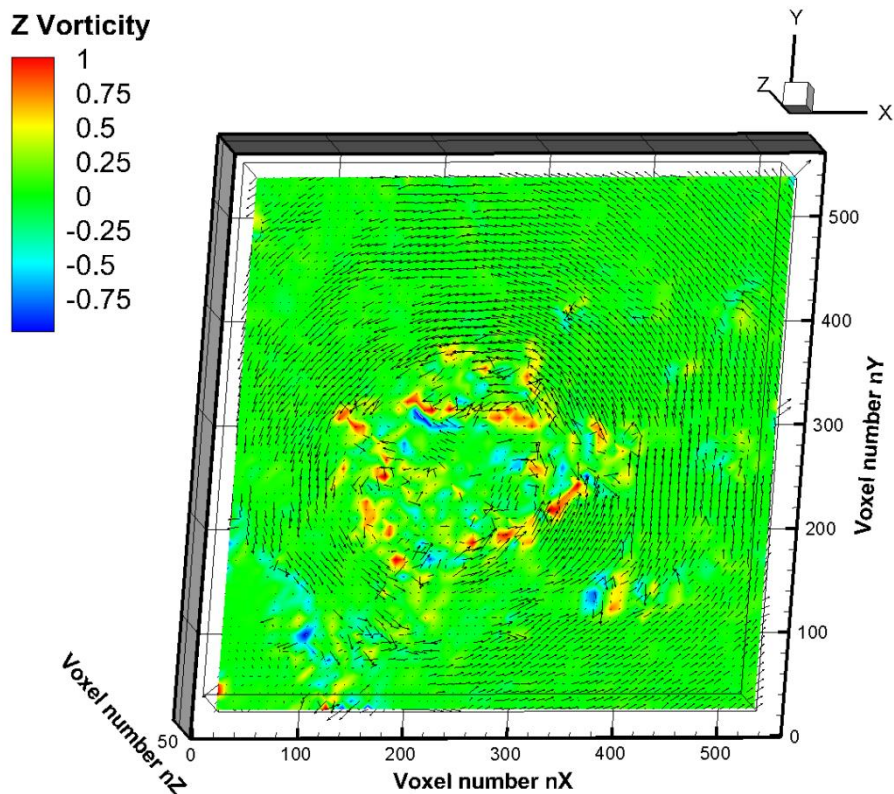
**Fig 4.6** Time evolution of tornado flow-rise of the reconstructed displacement vectors

Fig 4.6 shows the time evolution of the tornado flow at 1800 rpm motor speed and 0.06 depth ratio. The top view of middle Z-section and side view of Y-section of flow structures of the tornado flow is shown in Fig 4.6 (b)–(d) which depicts the stability and consistent uprising over time.

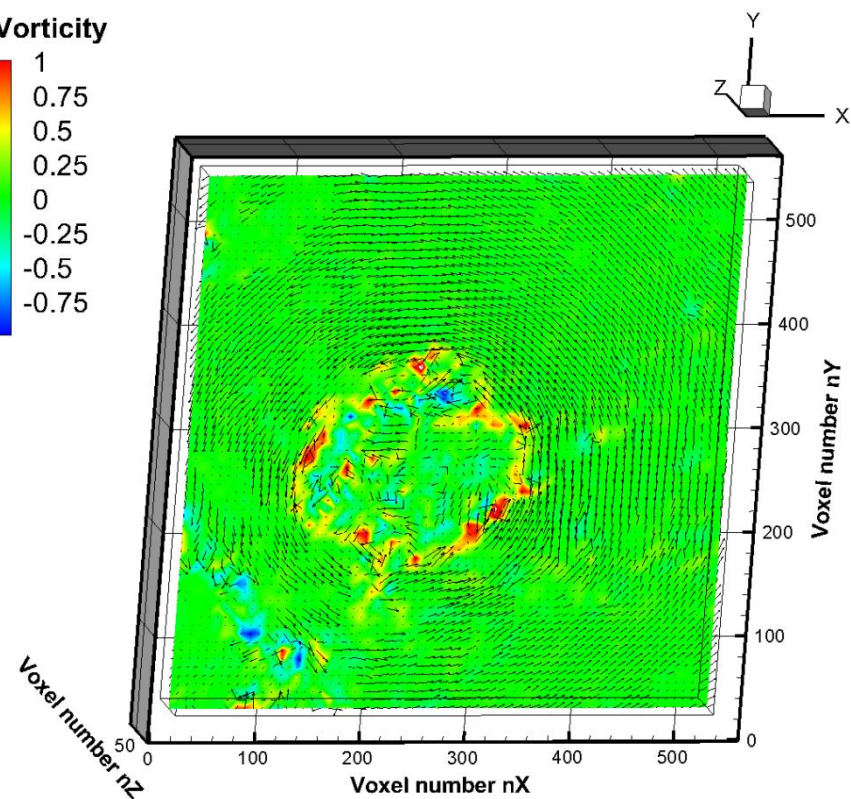
#### 4.4.3. Tornado flow characteristics at various heights



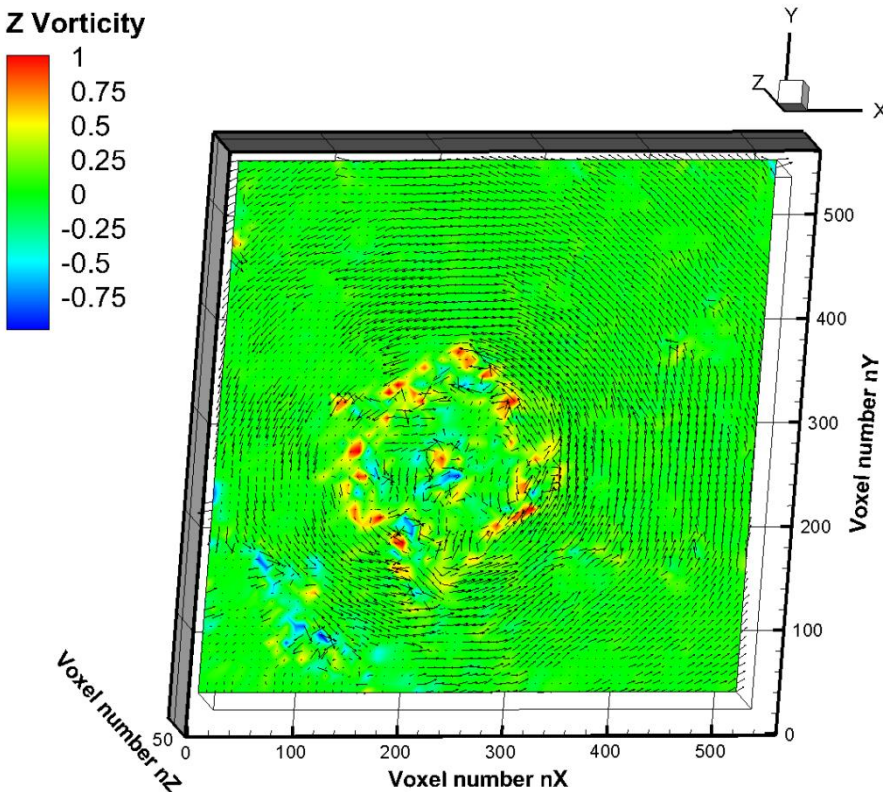
(a) conceptual schematic



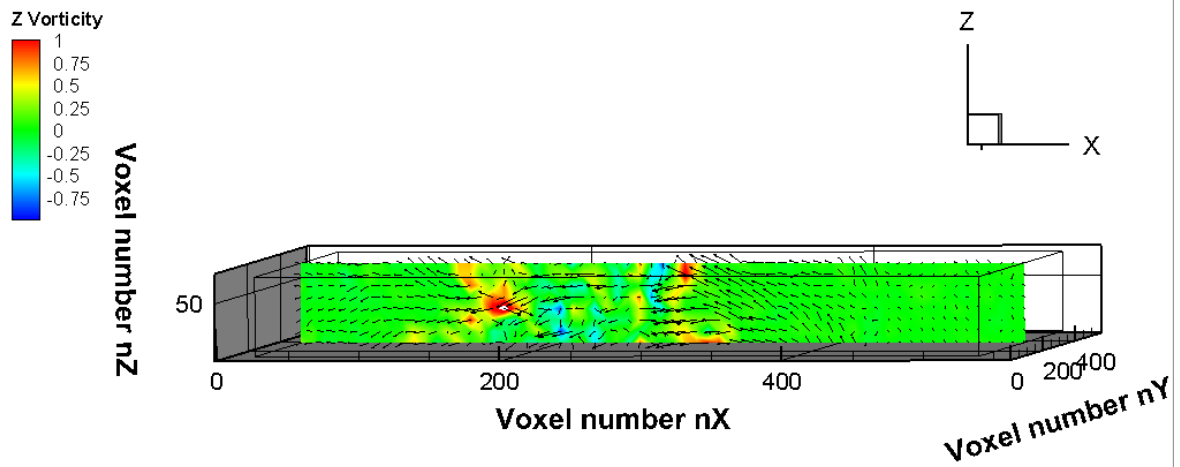
(b) bottom section



(c) middle section



(d) top section



(e) vertical section

**Fig 4.7** tornado flow-rise at different height sections of a water-tornado  
at a single time instant

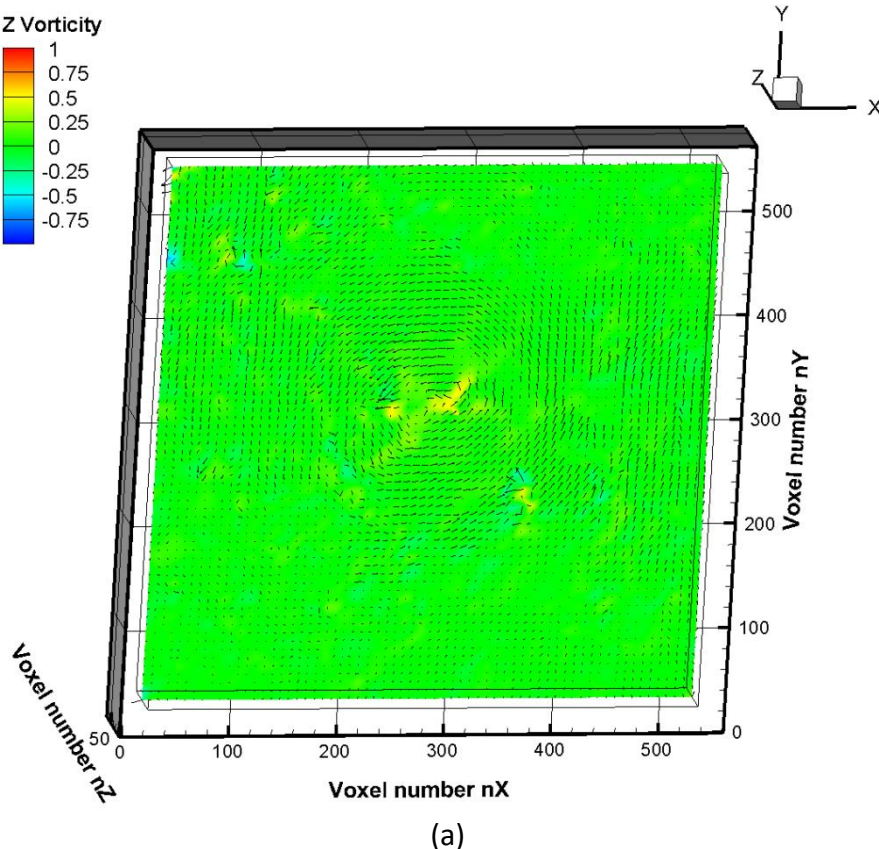
Fig 4.7 shows the flow characteristics of the tornado flow rise at bottom, mid and top section of tornado flow. The distribution of the maximum and minimum vorticity across the tornado periphery is more or less similar inferring to the fact that the tornado-rise is consistent at various layers which depicts the stability and consistent uprising across various cross-sections. Also a positive vorticity at the periphery and negative vorticity at the core throughout various layers indicate that the tornado flow is rising at the periphery and falling within the core. Also at a particular cross-section, mostly neutral (no rise) is observed in the

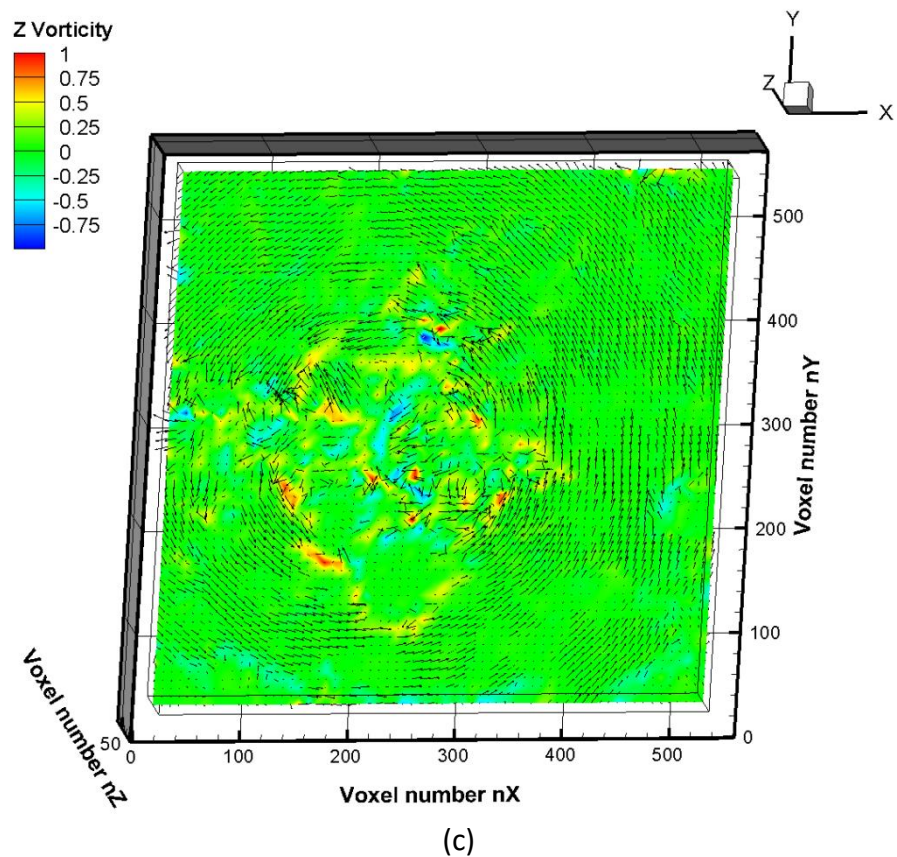
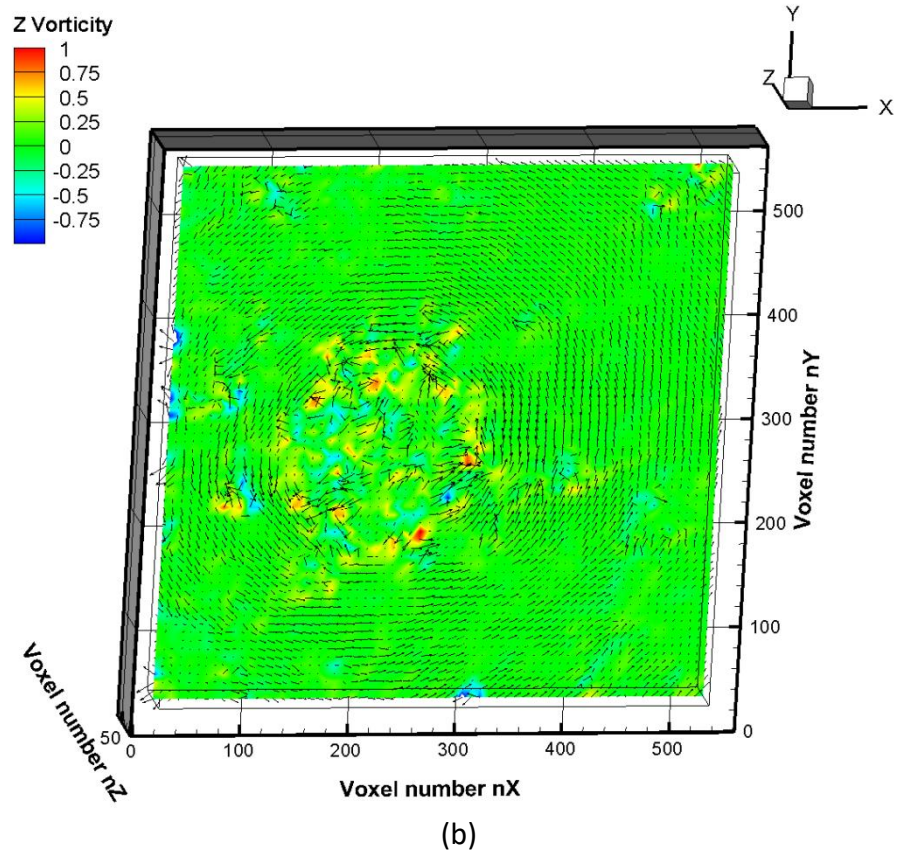
surrounding area whereas slight fluctuations are still present in some outer regions. This provides a good performance for minimum spread condition in PCS. The cross sectional velocity profiles of the water-tornado is not axisymmetric but rather oval with a small degree of circumferential undulation. And this undulation is not in phase along the axial direction of the water tornado as recognized from the two 2D cross sectional views at different observation height. This probably implies that the water tornado forms a helical structure of circumferential velocity undulation along its axis.

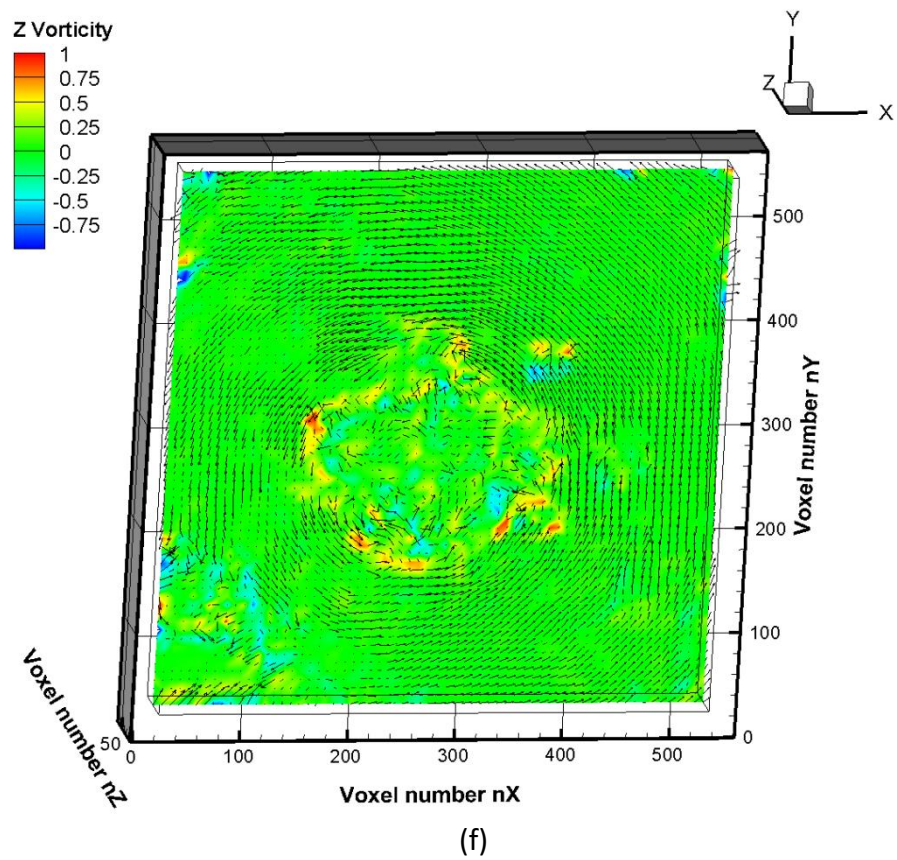
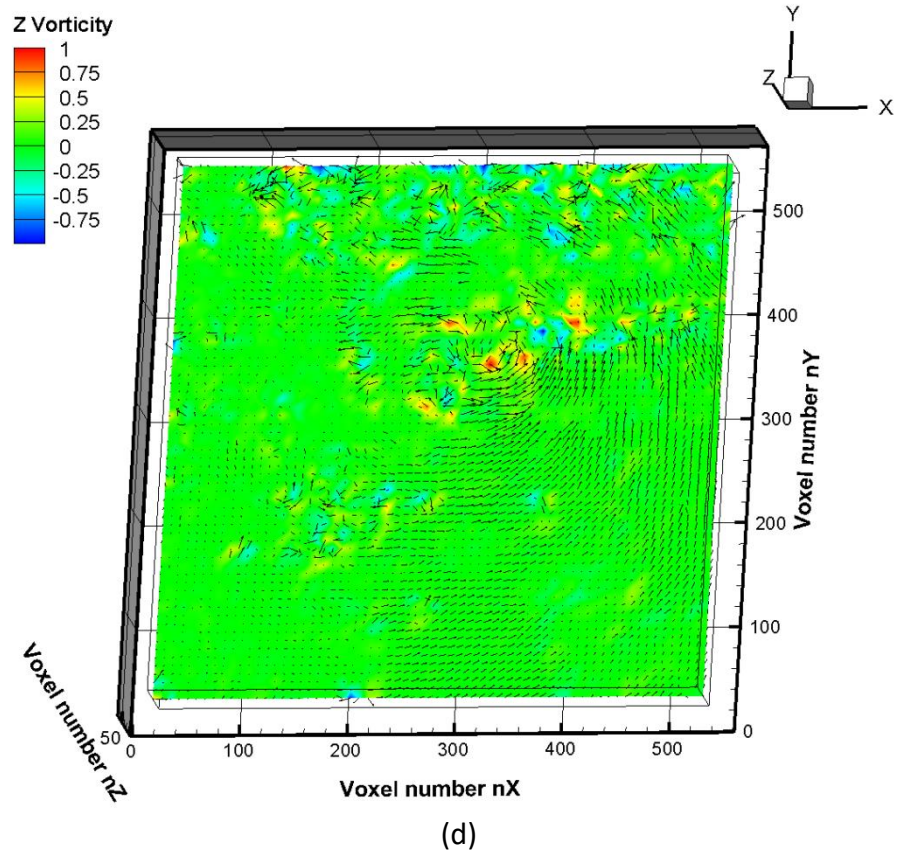
#### 4.5. Effects of motor speed

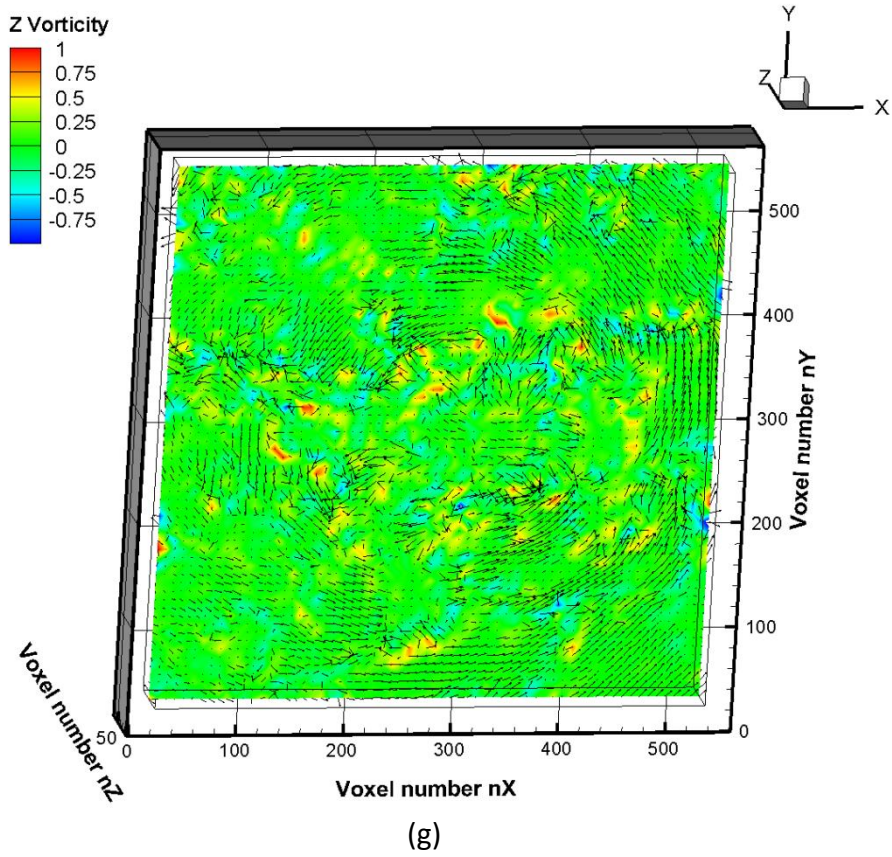
Fig 4.8 shows the tornado flow at different motor speeds 1000 - 2200 rotation per minute (rpm) in an interval of 200 rpm at a fixed 0.06 depth ratio. Other speeds lower than 1000 were not able to produce any tornado for proper extraction. The tornado began forming at speeds of 1000 rpm where small swirling action with minimum vorticity was present. With the rise of the motor speed from 1000 to 1800 rpm, the swirling action and the vorticity around the tornado ring increased as seen in Fig 4.8 (a)-(e) giving higher tornado-rise with minimum disturbance in the surrounding. Above 1800 rpm, the tornado-rise increased by very small amount but the surrounding disturbance was much higher as seen in Fig 4.8 (f)-(g). Time evolution of tornado-rise at 1000 rpm was also found to be the most stable.

Since the contamination of nearby regions during the sediment extraction process is of great concern in PCS, higher speeds even though they contribute more to tornado-rise is not favored. The motor speed of 1800 rpm is considered an optimum value due to its highest tornado-rise characteristics with minimum spread across the volume.

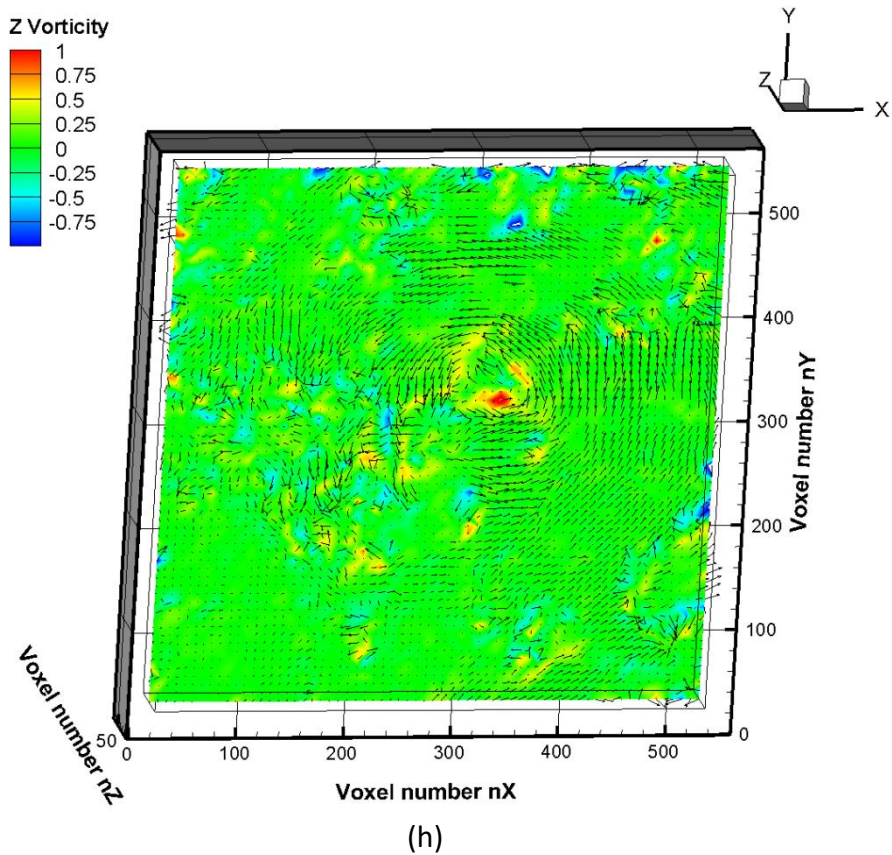








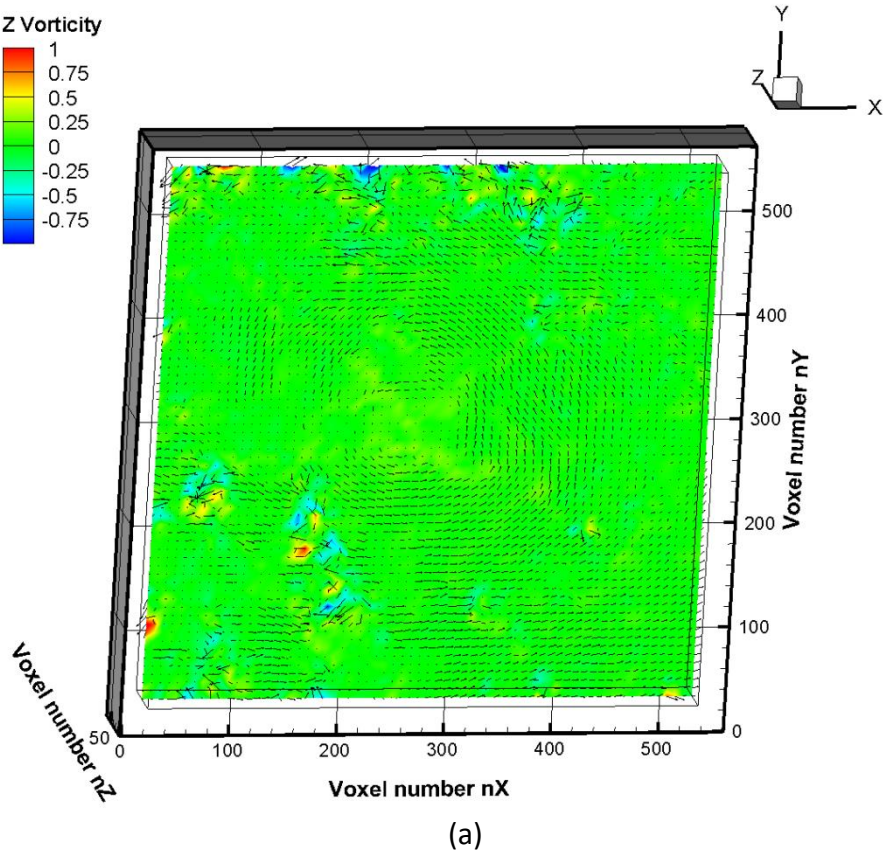
(g)



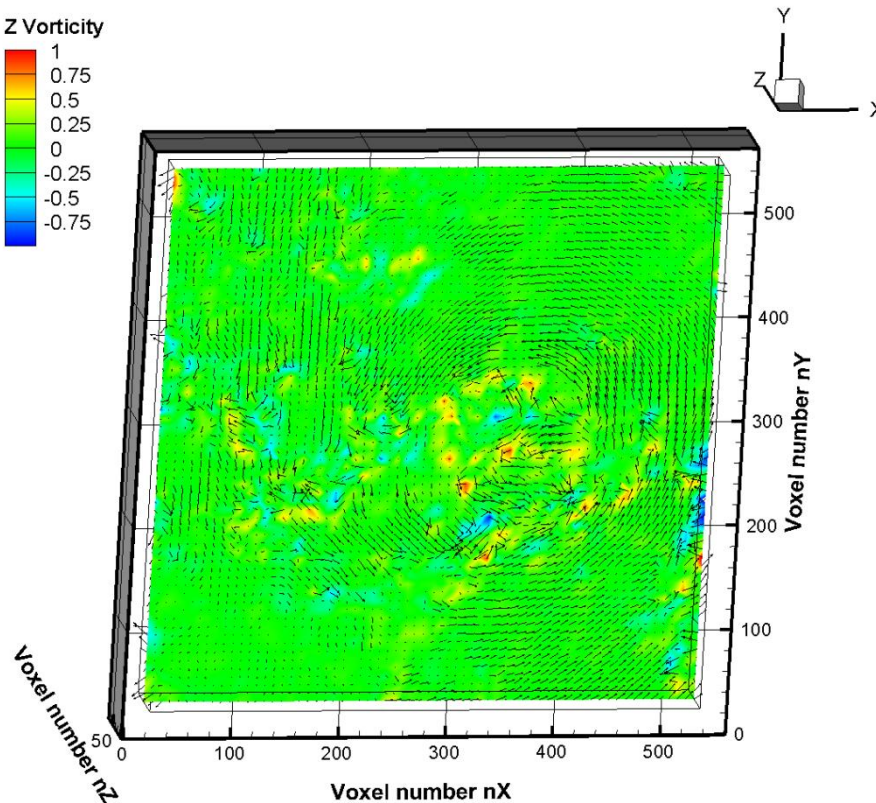
(h)

**Fig 4.8** tornado flow-rise at different motor speeds  
 (a) 1000 (b) 1200 (c) 1400 (d) 1600 (e) 1800 (f) 2000 (g) 2200 rpm

## 4.6. Effects of immersed impeller depth



(a)



(b)

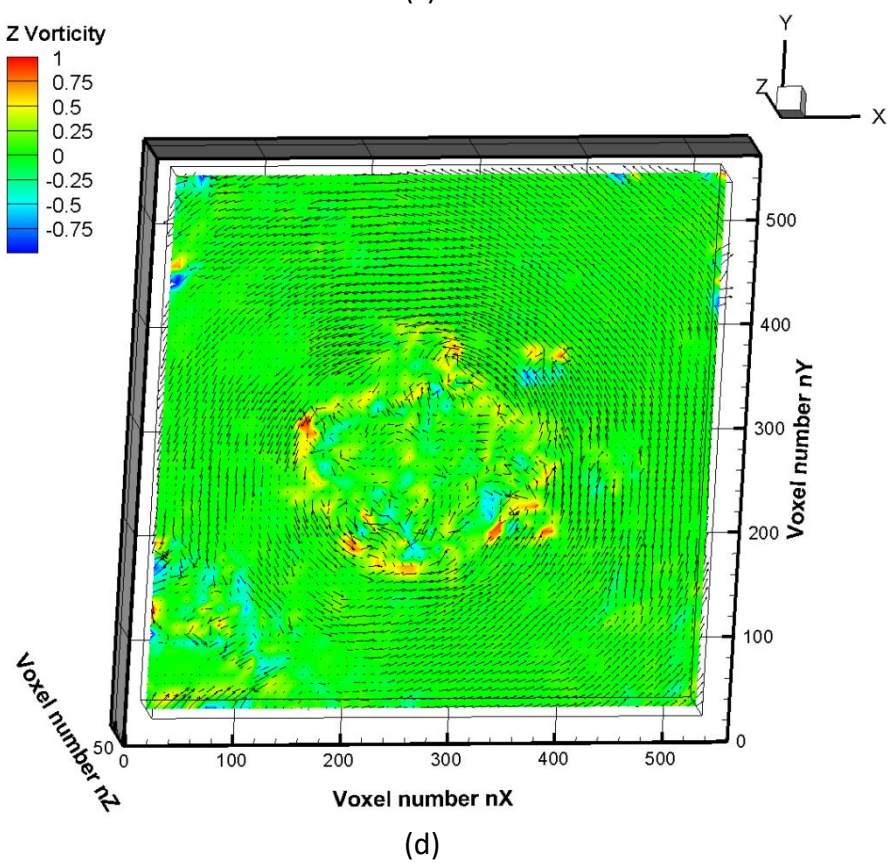
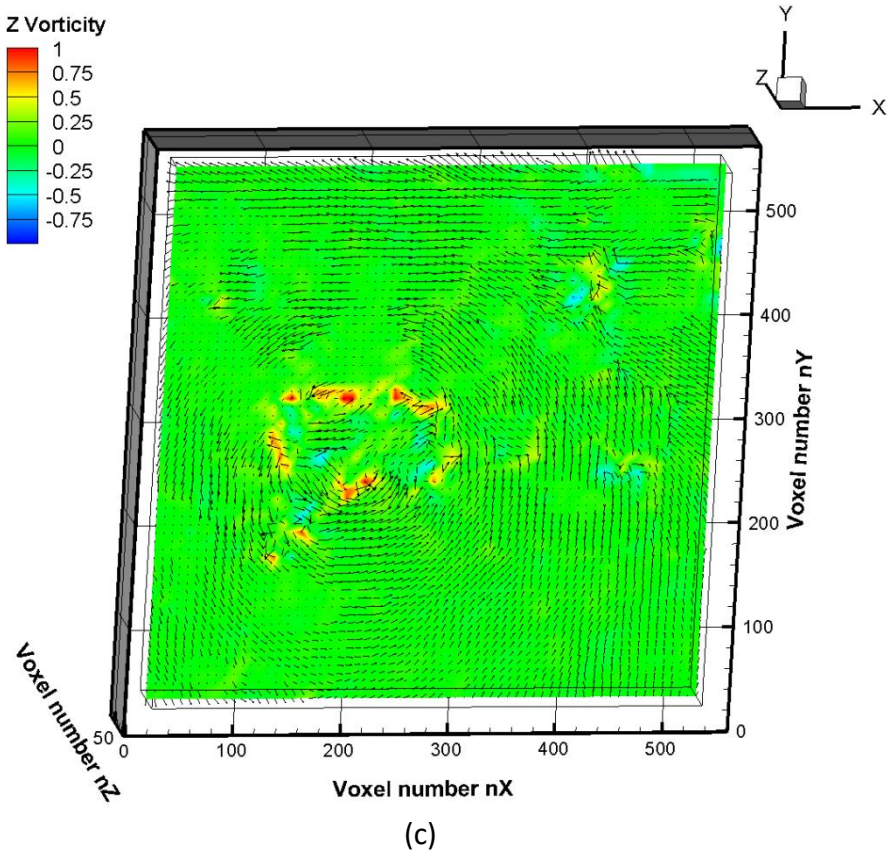


**Fig 4.9** tornado flow-rise at different immersed depth ratio

(a) 0.03 (b) 0.04 (c) .05 (d) .06

Fig 4.9 shows the tornado flow at different immersed depth ratio .03 - .06 in an interval of .01 at the most optimum motor-speeds of 1800 rpm. Impeller depths ratio of less than 0.03 were practically not feasible due to insufficient clearance between the impeller and the water tank cap causing lots of air cavitation preventing smooth operation of the impeller. Also due to limitation of the available impeller design, the depth ratio was limited to 0.06. The small tornado flow-rise formation started from 0.03 as shown in Fig 4.9 (a) which is not sufficient to produce enough flow-rise for proper extraction. Fig 4.9 (b)-(d) shows the gradual increase in the flow-rise as the immersed depth progressed. In case of immersed impeller depth, it was observed that the spread is high if the depth is low and vice-versa. The maximum available depth ratio .06 was found to have most stable tornado-rise flow characteristics.

For the optimum motor speed of 1800 rpm, the maximum available immersed impeller depth ratio of .06 is considered an optimum value due to its highest tornado-rise characteristics with minimum spread across the volume.

## 5. Conclusions

In this study, a full 3D-3C analysis of the water flow structure of a water tornado flow rise induced by subsurface rotating impeller in Powered water Circulatory system was performed using Tomographic PIV technique. The flow visualization results from the technique were utilized to understand vortex flow development of an artificial tornado flow generated by a rotating subsurface impeller for efficient pump-up circulation under various design parameters of the system.

The flow characteristics during full development and post breakdown stages were shown in the positional reconstructions. The highly increased circumferential velocity areas formed along the outer edge of the rotating water tornado were shown in the velocity reconstructions. The cross-sectional velocity of water tornado was found to be not axisymmetric but rather oval with a small degree of circumferential undulation.

Various experiments varying design parameters such as motor speeds (1000 – 2200 rpm) and immersed impeller depth ratio (.03-.06) were carried out for a water tornado-flow rise in a Powered water Circulatory System. Flow visualization technique was utilized to investigate the flow characteristics of tornado-rise at different heights of the tornado over time. Taking into consideration the sustainability of tornado and the highest tornado-flow rise with minimum spread, the optimum design parameters in a Powered water Circulatory System was found to be 1800 rpm motor speed with .06 immersed impeller depth ratios.

Thus, the Tomographic PIV technique was found to be very helpful and effective technique to investigate the characteristics of the water flow structure of a water tornado-flow rise in a Powered water Circulatory System.

# References

- [1]. ELSINGA G.E., SCARANO F., WIENEKE B., VAN OUDHEUSDEN B.W.: Tomographic particle image velocimetry, *6th International Symposium on Particle Image Velocimetry* (2005).
- [2]. HIRATSUKA A., ISHIKAWA M.: Development of UV sensor for the reservoir water quality evaluation and its application (in Japanese), *Journal of Japan Society of Civil Engineers*, **39**, 511-518 (2002).
- [3]. HANARI T., SAKAKIBARA J.: Dual-plane stereo-PIV study on tornado-like vortex in water (in Japanese), *Journal of Visualization Society Japan*, **30**(7), 47-54 (2010).
- [4]. OHMI K., HIRATSUKA A., SASAKI M.: Visualization experiment on an artificial tornado flow under density stratified water environment Particle Image Velocimetry, *Proceedings of 12th Asian Symposium on Visualization* (2013).
- [5]. Environment Measurement Services Inc.: EcoFlow Document (2009).  
<http://www.ems-kankyo.co.jp/ecoflow/en-punhu.pdf>
- [6]. ZHANG Z.: A Flexible New Technique for Camera Calibration, *IEEE Transactions on Pattern Analysis and Machine Intelligence*. **22**(11), 1330–1334 (2000).
- [7]. ROBERT COLLINS: Computer Vision I Fall 2007 Course, CSE486, Penn State.
- [8]. Kwon3d Courses: <http://kwon3d.com/theory/dlt/dlt.html>
- [9]. AVINASH C. KAK, MALCOLM STALEY: Principles of Computerized Tomographic Imaging, *Applied Mathematics*.
- [10]. HERMAN G.T., LENT A.: Iterative reconstruction algorithm, *Computers in Biology and Medicine*, **6**(4), 273-294 (1976).
- [11]. ATKINSON C. H., SORIA J.: Algebraic reconstruction techniques for Tomographic Particle Image Velocimetry, *16<sup>th</sup> Australian Fluid Mechanics Conference* (2007).
- [12]. BILSKY A., DULIN V., LOZHKNIN V., MARKOVICH D., TOKAREV M.: Two-dimensional Correlation Algorithms for Tomographic PIV, *9<sup>th</sup> International Symposium on Particle Image Velocimetry* (2011).
- [13]. NOBACH H., DAMASCHKE N., TROPEA C.: High-precision sub-pixel interpolation in PIV/PTV image-processing